TISSUE REGENERATION

Defective cholesterol clearance limits remyelination in the aged central nervous system

Ludovico Cantuti-Castelvetri,[1,2,3,4]* Dirk Fitzner,[1,5]* Mar Bosch-Queralt,[1,2,3,4] Marie-Theres Weil,[1,6] Minhui Su,[1,2,3,4] Paromita Sen,[1] Torben Ruhwedel,[7] Miso Mitkovski,[8] George Trendelenburg,[5] Dieter Lütjohann,[9] Wiebke Möbius,[6,7] Mikael Simons[1,2,3,4]†

Age-associated decline in regeneration capacity limits the restoration of nervous system functionality after injury. In a model for demyelination, we found that old mice fail to resolve the inflammatory response initiated after myelin damage. Aged phagocytes accumulated excessive amounts of myelin debris, which triggered cholesterol crystal formation and phagolysosomal membrane rupture and stimulated inflammasomes. Myelin debris clearance required cholesterol transporters, including apolipoprotein E. Stimulation of reverse cholesterol transport was sufficient to restore the capacity of old mice to remyelinate lesioned tissue. Thus, cholesterol-rich myelin debris can overwhelm the efflux capacity of phagocytes, resulting in a phase transition of cholesterol into crystals and thereby inducing a maladaptive immune response that impedes tissue regeneration.

Remyelination restores rapid transmission of nerve impulses and axonal function in the central nervous system (CNS) of patients with demyelinating diseases such as multiple sclerosis (MS). Although remyelination can occur in MS, age-associated decline in myelin repair contributes to chronic progressive disease and disability (*1*). Thus, understanding the cause of and preventing this decline are key goals in regenerative medicine (*2*–*4*). So far, epigenetic changes within aging oligodendrocyte progenitor cells and declines in phagocytic capacity of aged blood-derived monocytes have been identified as possible mechanisms (*5*, *6*). We implemented a toxin-induced model, in which a single injection of lysolecithin (lysophosphatidylcholine) induces a focal demyelinating lesion in the white matter of the brain or spinal cord of mice. In lesioned animals, demyelination is complete within 4 days, followed by a repair process that is maximal between 14 and 21 days postinjection (dpi) and requires rapid clearance of damaged myelin for regeneration to occur (*7*).

[1]Max Planck Institute of Experimental Medicine, 37075 Göttingen, Germany. [2]Munich Cluster for Systems Neurology (SyNergy), 81377 Munich, Germany. [3]Institute of Neuronal Cell Biology, Technical University Munich, 80805 Munich, Germany. [4]German Center for Neurodegenerative Disease (DZNE), 81377 Munich, Germany. [5]Department of Neurology, University of Göttingen Medical Center, 37075 Göttingen, Germany. [6]Center for Nanoscale Microscopy and Molecular Physiology of the Brain (CNMPB), 37075 Göttingen, Germany. [7]Department of Neurogenetics, Max Planck Institute of Experimental Medicine, 37075 Göttingen, Germany. [8]Light Microscopy Facility, Max Planck Institute of Experimental Medicine, 37075 Göttingen Germany. [9]Institute for Clinical Chemistry and Clinical Pharmacology, University of Bonn, 53127 Bonn, Germany.
*These authors contributed equally to this work.
†Corresponding author. Email: msimons@gwdg.de

We induced focal demyelinating lesions in the corpus callosum of young (3 months) and old (12 months) mice by lysolecithin injections. Lesions were of similar size at 4 dpi but not at 14 dpi, confirming the poor regenerative capacity of old mice (Fig. 1, A to C, and fig. S1, A to E). Sustained immune infiltration, as determined by IBA1-positive and MAC2-positive cells, was detected in old mice at 14 dpi (Fig. 1, A and E, and fig. S1G). Myelin debris accumulation within lysosomes of phagocytes (Fig. 1, D and F) and numerous foam cells harboring lipid droplets and needle-shaped cholesterol crystals—a typical hallmark of cholesterol overloading—were found in old mice (Fig. 1, G and H, and fig. S2G). Moreover, by a combination of laser reflection and fluorescence confocal microscopy (reflection microscopy) we confirmed the increase of crystal deposition in spinal cord lesions of old mice (Fig. 1, I and J). Crystals were similarly observed in two other models of myelin injury (fig. S2).

Toxic overload of cholesterol drives the formation of foamy macrophages and maladaptive immune responses in atherosclerosis. We hypothesized that the accumulation of cholesterol, the major component of myelin, may overwhelm the cholesterol transport capacity of phagocytes, thereby forming a bottleneck for successful repair in the aged CNS. Because cholesterol cannot be broken down, it must be transferred from the phagocytes back to the extracellular space via the transporters ABCA1 and ABCG1 [adenosine triphosphate–binding cassette (ABC) A1 and G1] in the plasma membrane where it binds high-density lipoprotein particles [e.g., apolipoprotein E (APOE)] (*8*). Real-time quantitative reverse transcription polymerase chain reaction (PCR) analyses revealed that the expression of *ApoE*, *Abca1*, and *Abcg1* was reduced in 4-dpi lesions of old mice compared with young mice (Fig. 1, K to M, and fig. S3). Oxysterols (hydroxylated cholesterol metabolites) such as 24*S*- and 27-hydroxycholesterol are endogenous ligands for the liver X receptor (LXR), thereby controlling the expression of genes involved in cholesterol efflux in cholesterol-loaded cells (*9*). Relative amounts of 24*S*-hydroxycholesterol did not differ in lesions of young and old animals, but 27-hydroxycholesterol levels were reduced in lesions of old mice (fig. S3). One possible explanation for lesion restitution failure in old mice is the inability to clear excessive myelin-derived cholesterol from phagocytes. Thus, we examined whether the LXR agonist GW3965 (*10*) improve lesion recovery in old mice by inducing the expression of genes involved in lipid efflux, such as *Abca1*, *Abcg1*, and *ApoE* (fig. S3). GW3965 led to markedly improved lesion regeneration in old mice, with a reduction in the number of IBA1-positive and MAC2-positive phagocytes (Fig. 1, A to C). In addition, the number of phagocytes containing myelin debris, the number of foam cells, and the amount of cholesterol crystals were reduced by treatment with GW3965 (Fig. 1, A to J).

Because accumulation of cholesterol in phagocytes may pose a barrier for successful tissue regeneration, we analyzed the regenerative capacity of mouse mutants lacking central factors of the reverse cholesterol transport pathway. We induced demyelinating lesions in 3-month-old NR1H3 (or LXRα) knockout (KO) mice and observed, as in aged wild-type (WT) mice, impaired lesion restitution and sustained phagocyte infiltration at 21 dpi (fig. S4, A to C). In addition, we detected accumulation of myelin debris in lysosomes of phagocytes and crystal deposition in lesions of LXRα KO mice (fig. S4, D to G).

Next, we analyzed the role of APOE, the major CNS cholesterol carrier that supports lipid efflux from cells (*11*). We induced focal demyelination in the corpus callosum of 12-week-old APOE KO and WT control mice and quantified lesion size and recovery. Lesion size did not differ initially, at 4 dpi (fig. S4, H to J). However, when lesions were analyzed at 21 dpi, we observed impaired lesion restitution. We detected increased numbers of IBA1-positive, MAC2-positive, and major histocompatibility complex class II (MHC II)–positive phagocytes, as well as enhanced crystal deposition and myelin debris accumulation within lysosomes of phagocytes in spinal cord and corpus callosum lesions of APOE KO animals as compared with control mice (Fig. 2 and fig. S5). Because APOE has functions beyond cholesterol transport (*11*), we tested the efficacy of cyclic oligosaccharide 2-hydroxypropyl-β-cyclodextrin (HβCD), a compound that increases cholesterol efflux and solubility (*12*), and found that HβCD treatment attenuated the phenotype of APOE KO animals (Fig. 3 and fig. S6).

Together with *Abca1* and *Abcg1*, *ApoE* represents one of the major nuclear LXR–regulated genes involved in mediating cholesterol efflux from phagocytes. We thus crossbred CX3CR1CreER animals with $Abca1^{fl/fl}$ and $Abcg1^{fl/fl}$ mice to obtain microglia- and macrophage-specific double-KO mice (ABCA1 and ABCG1 KO). We observed

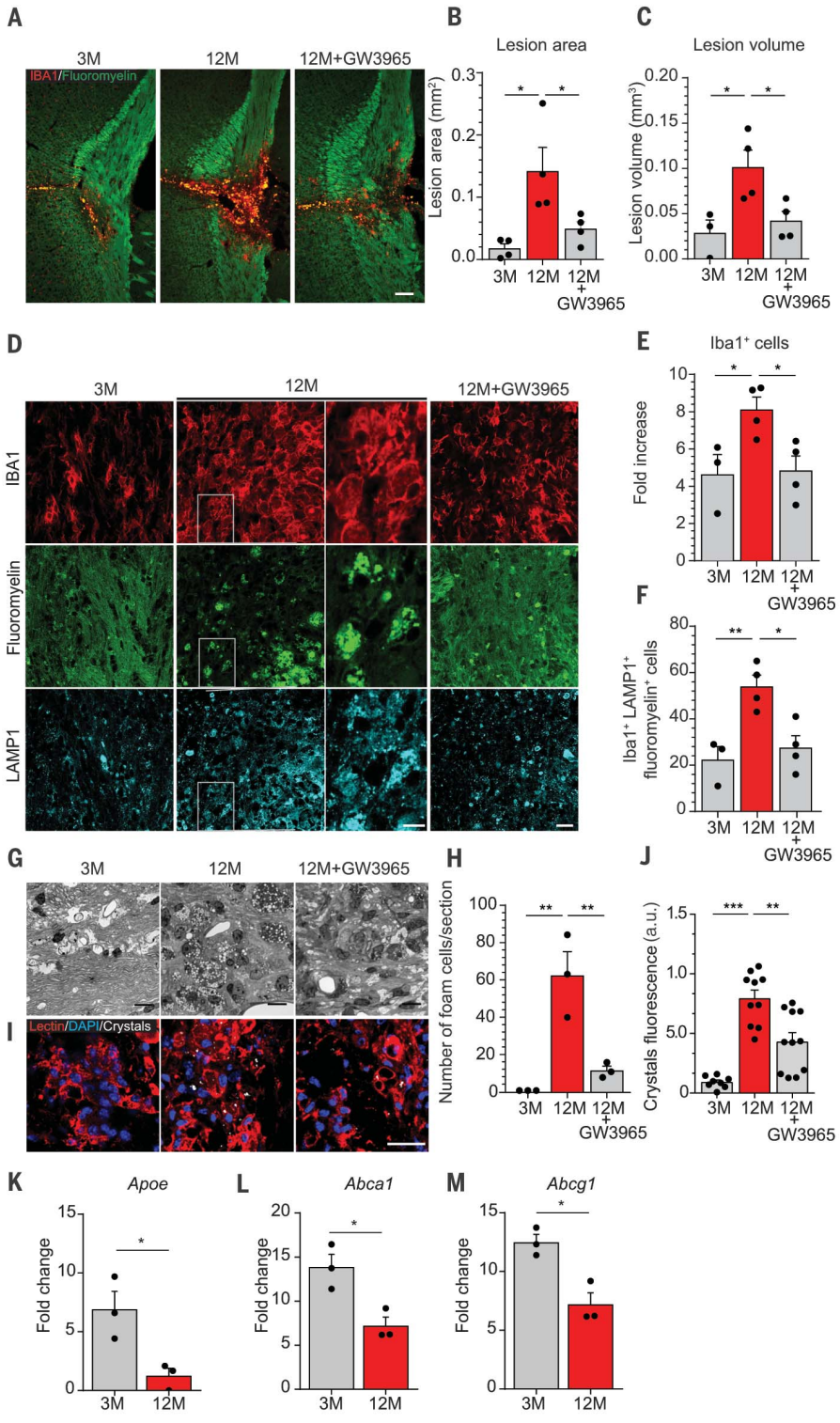

Fig. 1. Defective cholesterol clearance limits lesion regeneration in aged mice. (**A**) Images of corpus callosum lesions stained with fluoromyelin (green) and IBA1 (red) in 3-month-old (3M), 12-month-old (12M), and 12-month-old mice treated with GW3965 (12M+GW3965) at 14 dpi. Scale bar, 100 μm. (**B** and **C**) Quantification of lesion area in square millimeters, determined by luxol fast blue (LFB) staining, and in cubic millimeters, determined by fluoromyelin staining, at 14 dpi. (**D**) Confocal images of 3M, 12M, and 12M+GW3965 corpus callosum lesions showing IBA1 (red), fluoromyelin (green), and LAMP1 (blue). Scale bars, 40 μm. For 12M animals, the panels at right are magnified images of the boxed areas at left. (**E**) Change in number of IBA1$^+$ cells in corpus callosum lesions compared with the contralateral unlesioned side. (**F**) Number of IBA1$^+$, fluoromyelin$^+$, and LAMP1$^+$ cells in lesioned corpus callosum tissue at 14 dpi. (**G**) Semithin sections and (**H**) quantification of foam cells of 3M, 12M, and 12M+GW3965 corpus callosum lesions. Scale bars, 10 μm. (**I**) Reflection microscopy images of spinal cord lesions, showing crystals (white) in lectin$^+$ phagocytes (red), and (**J**) relative quantification of the fluorescence intensity of the reflected light. Scale bar, 25 μm. DAPI, 4′,6-diamidino-2-phenylindole; a.u., arbitrary units. (**K** to **M**) Quantitative PCR analysis of *Apoe*, *Abca1*, and *Abcg1* in 4-dpi lesions of 3M and 12M mice. All data are mean ± SEM (error bars); **P* < 0.05, ***P* < 0.01, ****P* < 0.001 by one-way analysis of variance (ANOVA) test, with Tukey's multiple comparison test.

an increased number of IBA1-positive and MHC II–positive phagocytes, an increase in crystal deposition, and fewer myelinated axons in 21-dpi lesions of ABCA1 and ABCG1 KO animals as compared with controls (fig. S7).

Because excessive cholesterol accumulation in phagocytes limits lesion recovery, we turned to cell culture experiments to determine the mechanisms involved. We prepared phagocytes [primary microglia or bone marrow–derived macrophages (BMDMs)] from APOE KO and WT mice and examined the phagocytic uptake of myelin debris, which did not differ in cells prepared from WT or APOE KO mice (fig. S8, A and B). Because APOE is also produced by astrocytes, we incubated cells in the presence of serum-free conditioned media prepared from either WT or APOE KO astrocytes and observed the clearance of the internalized myelin particles from phagocytes. Myelin debris persisted within lysosomes of APOE KO cells that were incubated with conditioned media from APOE KO astrocytes. Clearance could be improved by an APOE-derived mimetic peptide, ATI5261 (*13*), which contains an amphipathic α-helical motif responsible for lipid binding and cholesterol efflux (Fig. 3, E and F). Moreover, myelin debris treatment

resulted in crystal formation, which was increased in APOE KO macrophages and reduced by GW3965 treatment (fig. S8, C to G).

In atherosclerosis, cholesterol crystals can induce inflammation by phagolysosomal membrane rupture and subsequent stimulation of the caspase-1–activating NLRP3 (NALP3 or cryopyrin) inflammasome and secretion of interleukin (IL)–1 cytokines (*14*, *15*). Myelin debris treatment resulted in lysosomal permeabilization and caspase-1 cleavage in WT but not in NLRP3-deficient macrophages (Fig. 4, A to H, and fig. S9, A and B). More pronounced caspase-1 activation was observed in APOE KO as compared with WT macrophages, which was confirmed in vivo in APOE KO mice after lysolecithin injection (Fig. 4E and fig. S9C). Myelin overloading induced cell death, which resulted in DNA fragmentation [detected by TUNEL (terminal deoxynucleotidyl transferase–mediated deoxyuridine triphosphate nick end labeling) assay], was cholesterol dependent (fig. S9, D and E), and was rescued by caspase-1 inhibitors, pointing to an inflammasome-mediated pyroptotic cell death pathway (Fig. 4G and fig. S10). Thus, cholesterol derived from myelin debris can activate the NLRP3 inflammasome in macrophages when toxic levels build up intracellularly in the absence of sufficient lipoprotein carriers.

Because jamming the lysosomal system with myelin debris resulted in cholesterol crystallization and inflammasome activation, we asked whether this pathway was responsible for limiting regeneration in old mice. To examine whether increased inflammasome activation contributed to the poor recovery of old mice, we

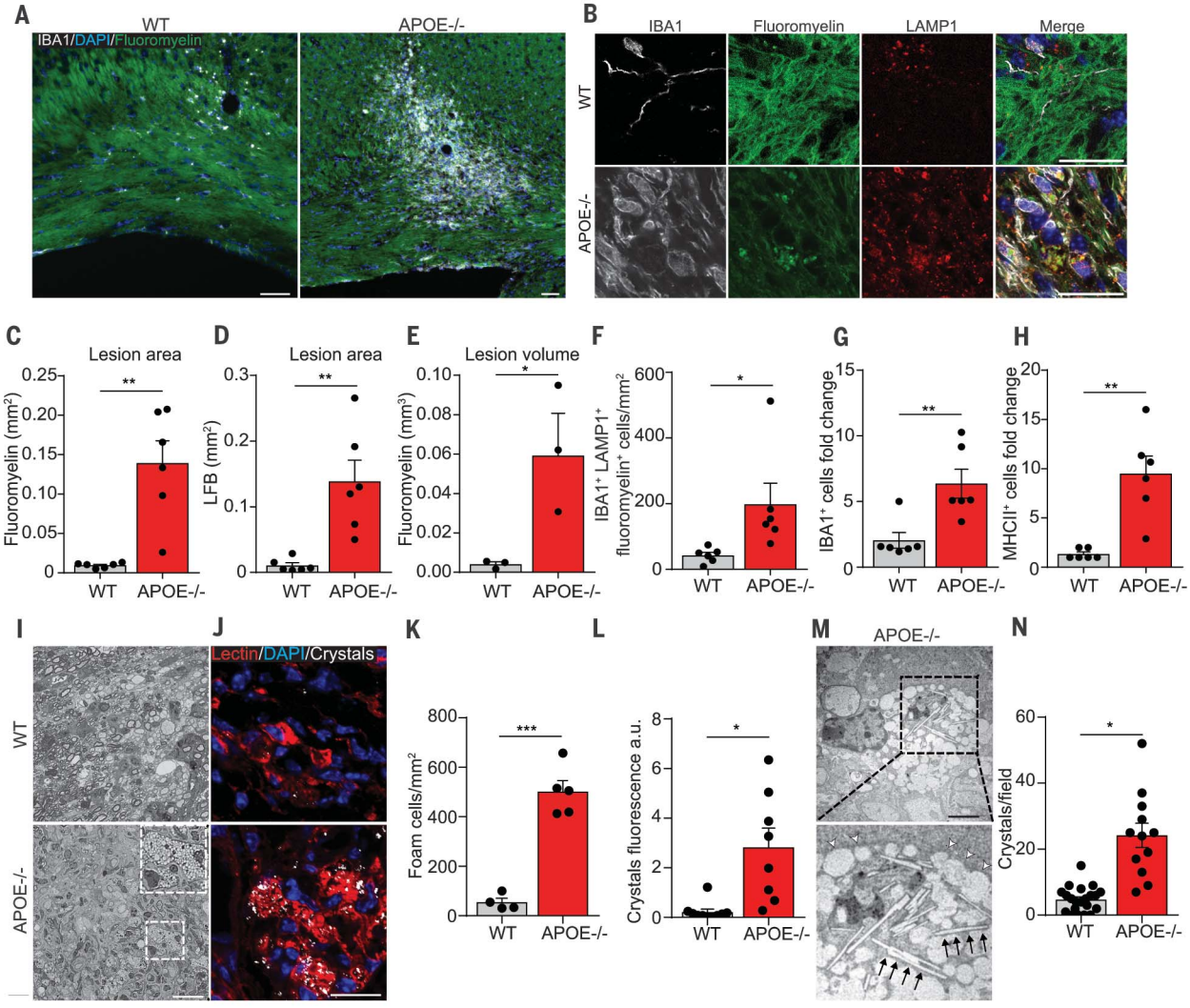

Fig. 2. APOE is required for cholesterol clearance in demyelinating lesions. (**A** and **B**) Images of corpus callosum lesions in WT and APOE$^{-/-}$ mice at 21 dpi showing fluoromyelin staining (green), IBA1 (white), DAPI (blue), and LAMP1 (red). (**C** and **D**) Quantification of lesion area in square millimeters at 21 dpi, as determined by fluoromyelin and LFB staining. (**E**) Lesion volume in cubic millimeters, as measured by fluoromyelin staining in consecutive sections. (**F**) Number of IBA1$^+$, fluoromyelin$^+$, and LAMP1$^+$ cells per square millimeters in lesions at 21 dpi. (**G** and **H**) Change in the number of IBA1$^+$ and MHC II$^+$ cells in the lesioned corpus callosum as compared with the contralateral unlesioned side. (**I**) Representative images (boxed area of bottom left panel shown at larger magnification in right corner) and (**K**) quantification of foam cells in spinal cord lesions in WT and APOE$^{-/-}$ mice at 21 dpi. (**J**) Reflection microscopy images of 21-dpi lysolecithin lesions, showing crystals (white) in lectin$^+$ phagocytes (red), and (**L**) relative quantification of the fluorescence intensity of the reflected light. (**M**) Transmission electron microscopy images of foam cells in 21-dpi lesions of APOE$^{-/-}$ mice (the boxed area is shown below at higher magnification), showing needle-like cholesterol crystals (black arrows) and lipid droplets (white arrowheads), and (**N**) relative quantification of crystals. All data are mean ± SEM (error bars); *P < 0.05, **P < 0.01, ***P < 0.001 by two-tailed Student's t test. Scale bars in (A), (B), (I), and (J), 25 μm; scale bar in (K), 2.5 μm.

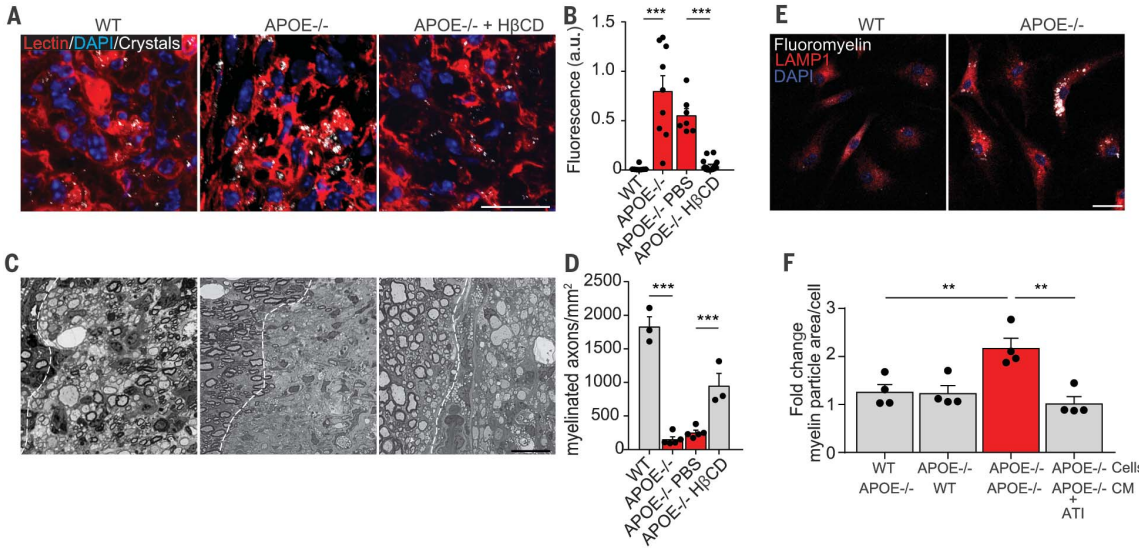

Fig. 3. Enhancing cholesterol clearance prevents lysosomal storage of myelin debris and crystal formation. (**A**) Representative images with crystals (white) and lectin^{+} phagocytes (red), and (**B**) quantification of cholesterol crystals in lysolecithin lesions of WT, APOE$^{-/-}$, and APOE$^{-/-}$ mice treated with HβCD or phosphate-buffered saline (PBS). Scale bar, 25 μm. (**C**) Representative images of methylenblue-azur II staining and (**D**) quantification of remyelination in lysolecithin lesions at 21 dpi. In (C), the edges of the lesions are identified by dashed lines. Scale bar, 25 μm. (**E**) Confocal images of primary microglial cell cultures prepared from WT or APOE$^{-/-}$ mice, treated with myelin debris and stained for LAMP1 (red), fluoromyelin (white), and DAPI (blue) at 24 hours posttreatment. Microglia from WT or APOE$^{-/-}$ mice were treated with myelin debris and subsequently transferred in media conditioned either by WT or APOE$^{-/-}$ astrocytes. APOE$^{-/-}$ microglia cells in APOE$^{-/-}$ conditioned media (CM) were additionally treated with APOE mimetic peptide (ATI). Scale bar, 25 μm. (**F**) Change in the area of myelin particles per cell as compared with WT cells in WT conditioned media. All data are mean ± SEM (error bars); $^{**}P < 0.01$, $^{***}P < 0.001$ by two-way ANOVA, with Tukey's multiple comparison test.

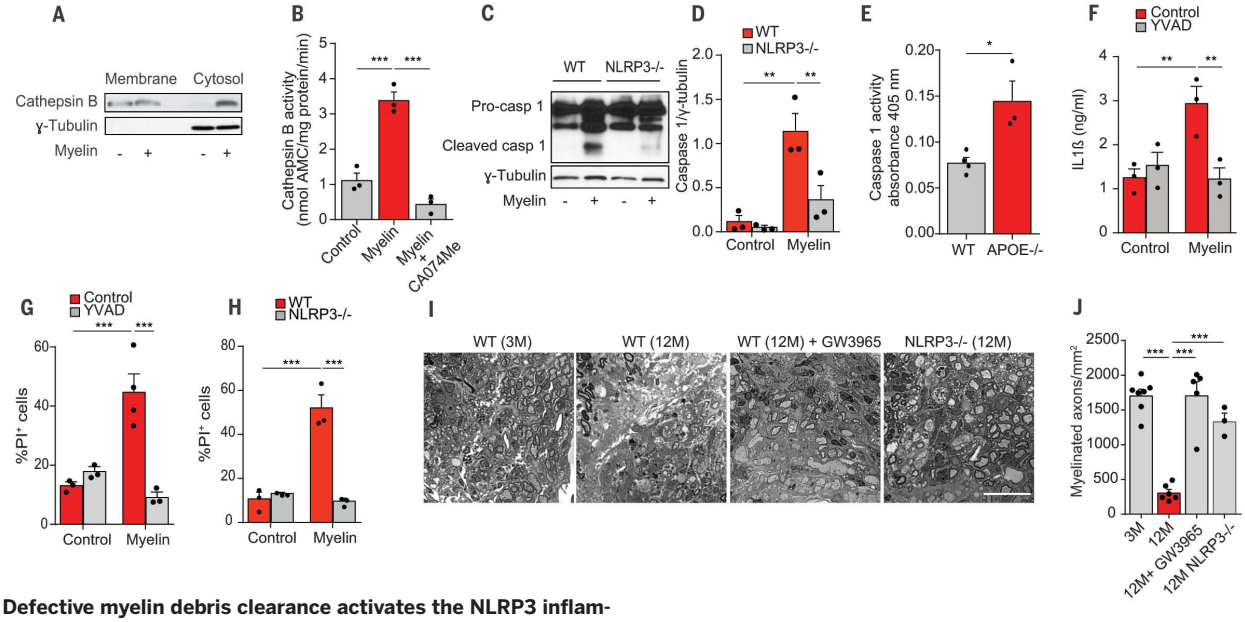

Fig. 4. Defective myelin debris clearance activates the NLRP3 inflammasome. (**A**) Immunoblot of cytosol and membrane fractions of primary BMDMs 12 hours after treatment with myelin debris for cathepsin B and γ-tubulin. (**B**) Cathepsin B activity assay of the cytosolic fraction of control macrophages 12 hours after treatment with myelin debris in the presence or absence of the cathepsin B inhibitor CA074me (10 μM). AMC, 7-amino-4-methylcoumarin. (**C** and **D**) Immunoblot and quantification of the active subunit of caspase 1 (p20) after myelin debris treatment of WT or NLRP3$^{-/-}$ BMDMs. The intensity of the p20 band was normalized to γ-tubulin. (**E**) Caspase 1 activity in lysates from lysolecithin lesions of WT and APOE$^{-/-}$ mice at 21 dpi. (**F**) Enzyme-linked immunosorbent assay for IL-1β release in WT BMDMs, after treatment with myelin debris with or without YVAD. (**G**) Quantification of the percentage of dead cells [propidium iodide–positive (PI^{+})] after myelin debris treatment (12 hours) in the presence or absence of a caspase-1 inhibitor (YVAD). (**H**) Quantification of PI^{+} cells after treatment of WT and NLRP3$^{-/-}$ BMDMs with myelin debris for 12 hours. (**I**) Methylenblue-azur II staining of remyelinating lesions in the spinal cord of 3M, 12M, GW3965-treated 12M, and 12M NLRP3$^{-/-}$ mice and (**J**) relative quantification of myelinated fibers. All data are mean ± SEM (error bars); $^{*}P < 0.05$, $^{**}P < 0.01$, $^{***}P < 0.001$ by one-way ANOVA test, with Tukey's multiple comparison test and two-tailed Student's *t* test (E). Scale bar in (I), 25 μm.

analyzed spinal cord lesions of aged WT and NLRP3-deficient mice. As in GW3965-treated old animals (Fig. 4, I and J), we found significantly improved remyelination in aged NLRP3-deficient mice as compared with aged WT mice at 21 dpi. Thus, inflammasome activation, possibly downstream of cholesterol accumulation, drives a maladaptive immune response that hampers inflammation resolution and repair in aged mice.

Self-resolving inflammation is essential for a proper restorative process after tissue damage, whereas uncontrolled inflammation can leave lasting marks that permanently alter tissue homeostasis (*16*). We made the surprising discovery that the self-limiting inflammatory response, which is necessary to initiate a regenerative process, is maladaptive in the CNS of aged mice. It appears that the inability of aged phagocytes to clear the enormous amounts of cholesterol that are released from myelin after myelin breakdown in demyelinating diseases results in a phase transition of free cholesterol into crystals, inducing lysosomal rupture and inflammasome stimulation, consistent with the beneficial effects of nuclear receptor agonists in remyelination (*17*, *18*). The unexpected link between lipid metabolisms and tissue regeneration provides opportunities for the development of regenerative medicines for remyelination and for improving functional recovery after CNS injury (*19*).

REFERENCES AND NOTES

1. P. Patrikios *et al*., *Brain* **129**, 3165–3172 (2006).
2. F. J. Najm *et al*., *Nature* **522**, 216–220 (2015).
3. F. Mei *et al*., *Nat. Med.* **20**, 954–960 (2014).
4. V. A. Deshmukh *et al*., *Nature* **502**, 327–332 (2013).
5. J. M. Ruckh *et al*., *Cell Stem Cell* **10**, 96–103 (2012).
6. S. Shen *et al*., *Nat. Neurosci.* **11**, 1024–1034 (2008).
7. V. E. Miron *et al*., *Nat. Neurosci.* **16**, 1211–1218 (2013).
8. K. J. Moore, I. Tabas, *Cell* **145**, 341–355 (2011).
9. X. Fu *et al*., *J. Biol. Chem.* **276**, 38378–38387 (2001).
10. C. Hong, P. Tontonoz, *Nat. Rev. Drug Discov.* **13**, 433–444 (2014).
11. R. W. Mahley, *Science* **240**, 622–630 (1988).
12. S. Zimmer *et al*., *Sci. Transl. Med.* **8**, 333ra50 (2016).
13. A. Hafiane, J. K. Bielicki, J. O. Johansson, J. Genest, *Biochim. Biophys. Acta* **1841**, 1498–1512 (2014).
14. P. Duewell *et al*., *Nature* **464**, 1357–1361 (2010).
15. K. Rajamäki *et al*., *PLOS ONE* **5**, e11765 (2010).
16. A. Aguzzi, B. A. Barres, M. L. Bennett, *Science* **339**, 156–161 (2013).
17. J. K. Huang *et al*., *Nat. Neurosci.* **14**, 45–53 (2011).
18. D. Meffre *et al*., *Proc. Natl. Acad. Sci. U.S.A.* **112**, 7587–7592 (2015).
19. F. Bei *et al*., *Cell* **164**, 219–232 (2016).

ACKNOWLEDGMENTS

We thank L. Vaculčiaková for help with the calculations of three-dimensional reconstructions and A. Kerksiek for technical assistance. This work was supported by a European Research Council (ERC) Consolidator Grant (M.S.) and grants from the German Research Foundation (DFG) (SI 746/9-1,10-1, SPP1757, TRR128, and TRR43), the Klaus Tschira Stiftung, the Adelson Foundation, Excellence Cluster for Systems Neurology (SyNergy), and Excellence Cluster for Nanoscale Microscopy and Molecular Physiology of the Brain (CNMPB). W.M. is supported by an ERC grant to K.-A. Nave. M.B.-Q. is supported by a Boehringer Ingelheim stipend. All data are presented in the main text and supplementary materials.

SUPPLEMENTARY MATERIALS

www.sciencemag.org/content/359/6376/684/suppl/DC1
Materials and Methods
Figs. S1 to S10
References (*20*–*29*)

10 April 2017; resubmitted 5 November 2017
Accepted 11 December 2017
Published online 4 January 2018
10.1126/science.aan4183

Defective cholesterol clearance limits remyelination in the aged central nervous system

Ludovico Cantuti-Castelvetri, Dirk Fitzner, Mar Bosch-Queralt, Marie-Theres Weil, Minhui Su, Paromita Sen, Torben Ruhwedel, Miso Mitkovski, George Trendelenburg, Dieter Lütjohann, Wiebke Möbius and Mikael Simons

Science **359** (6376), 684-688.
DOI: 10.1126/science.aan4183originally published online January 4, 2018

Keeping cholesterol at bay

A decline in tissue repair is a universal hallmark of aging. The failure to regenerate myelin sheaths in multiple sclerosis lesions contributes to chronic progressive disease and disability. Understanding the cause and preventing this failure is a key goal in regenerative medicine. Cantuti-Castelvetri *et al.* report that the self-limiting inflammatory response, which is necessary for remyelination to occur, is maladaptive in the central nervous system (CNS) of old mice (see the Perspective by Chen and Popko). Cholesterol-rich myelin debris overwhelmed the efflux capacity of phagocytes, resulting in a transition of free cholesterol into crystals, thereby inducing lysosomal rupture and inflammasome stimulation. Thus, drugs being developed to promote cholesterol clearance in human atherosclerosis lesions may also be good candidates for regenerative medicine in the CNS.

Science, this issue p. 684; see also p. 635

Science (print ISSN 0036-8075; online ISSN 1095-9203) is published by the American Association for the Advancement of Science, 1200 New York Avenue NW, Washington, DC 20005.

Supplementary Materials for

Defective cholesterol clearance limits remyelination in the aged central nervous system

Ludovico Cantuti-Castelvetri,* Dirk Fitzner,* Mar Bosch-Queralt, Marie-Theres Weil, Minhui Su, Paromita Sen, Torben Ruhwedel, Miso Mitkovski, George Trendelenburg, Dieter Lütjohann, Wiebke Möbius, Mikael Simons†

*These authors contributed equally to this work.
†Corresponding author. Email: msimons@gwdg.de

Published 4 January 2018 on *Science* First Release
DOI: 10.1126/science.aan4183

This PDF file includes:

Supplementary Materials

Material and Methods

Animals

All experiments were performed in accordance with the German animal welfare law and local regulations for animal experiments. The animals were kept in 12h light dark-cycles and bred in the animal facility of the Max Planck Institute of Experimental Medicine and the University Medical Center Göttingen. The ApoE knockout animals (*20*) were kindly provided by Tim Seidler (University of Göttingen, Germany) and the NLRP3 knockout animals were kindly provided by Nicolas Fasel (Department of Biochemistry, Switzerland), LXRα knockout animals (Nr1h3tm1Djm) and $Abca1^{fl/fl}$ and $Abcg1^{fl/fl}$ were purchased from Jackson Laboratories (*21*) (*22*). $Abca1^{fl/fl}$ and $Abcg1^{fl/fl}$ were crossed with mice with a tamoxifen inducible Cre-mediated recombination system (Cre-ERT2) driven by CX3CR1 promoter ($CX3CR1^{CreER}$ mice kindly provided by S. Jung, Weizmann Insitute, Israel (*23*)) to generate mice whose macrophages and microglia lacked ABCA1 and ABCG1. Tamoxifen (Sigma T5648) was dissolved in filter-sterilized corn oil to make solution of 10 mg/ml. The solution was protected from light, and placed on the roller mixer to be dissolved over night at 37°C. It was administrated via intraperitoneal injection once every 24 hours in 5 consecutive days. The injection dose was determined by weight, using approximately 75 mg tamoxifen/kg body weight. For adult mice, a standard dose of 100 µl tamoxifen/corn oil solution was effective to induce Cre recombinase activity. As control animals we used tamoxifen injected $CX3CR1^{CreERT/wt}$:$Abca1^{wt/wt}$:$Abcg1^{wt/wt}$ and vehicle (corn oil) injected $CX3CR1^{CreERT/wt}$:$Abca1^{fl/fl}$:$Abcg1^{fl/fl}$. Genotype for the animals lacking the NLRP3 protein was carried out with the following primers: forward 5'GCTCAGGACATACGTCTGGA; reverse for the WT 5'TGAGGTCCACATCTTCAAGG; reverse for the mutant 5'TTGTAGTTGCCGTCGTCCTT. Genotype for the animals deficient in APOE was carried out with the following primers; forward 5′-GCCTAGCCGAGGGAGAGCCG; reverse for the WT 5′-TGTGACTTGGGAGCTCTGCAGC; reverse for the knock out 5′-GCCGCCCCGACTGCATCT. Genotype for the animals deficient in LXRα was carried out with the following primers: forward 5'-TTG TGC CCA GTC ATA GCC GAAT; reverse for the WT 5'-TCA GTG GAG GGA AGG AAA TG; reverse for the mutant 5'-TTC CTG CCC TGG ACA CTT AC. Each animal line was kept on a pure C57BL/6 genetic background. For the injection of lysolecithin, animals (female and male) were anesthetized with a solution of

ketamine/xylazine solution (10 mg/ml ketamine and 1 mg/ml xylazine) and positioned into a stereotactic injection apparatus. For the corpus callosum injections, a hole was drilled and the capillary was positioned 0.1 mm posterior and 1.0 mm lateral to the bregma. The capillary was slowly lowered (1.36 mm) and 1 µl of 1% lysolecithin (Sigma-Aldrich, L4129) and a trace of Monastral blue (Sigma-Aldrich, 274011-50G) was injected at a rate of 150 nl/minute. 5 minutes after the delivery of the lysolecithin, the capillary was slowly retracted. The skin was then sutured. For the injection of lysolecithin in the spinal cord, the animals were anesthetized as above, the mouse dorsal skin was shaved and a 3 cm incision was performed. The dorsal muscles were cut and the connective tissue between T3 and T4 was removed, exposing the spinal cord. The capillary was then positioned 0.5 mm lateral to the dorsal artery and lowered 1.5 mm into the tissue. The delivery of lysolecithin and the retraction of the capillary were performed as above. Treatment with the LXR agonist GW3965 (Selleckchem, S2630) was performed by feeding animals with powdered standard rodent chow substituted with the compound to achieve continuous delivery of the drug. The amount of drug added was calculated according to daily food intake and weight of mice resulting in an average daily dose of 20mg/kg. Treatment was started two days ahead of the injection and treatment was continued for 4, 14 or 21 days. Treatment with HβCD (Sigma, H107) was performed by injecting subcutaneously a solution of 20% *w/v* of HβCD (400mg/kg of body weight) every 48 hours, starting on the day of the lysolecithin injection. PBS injections were used as control.

Myelin preparation

Myelin was isolated as previously described (*24*). Briefly, 8-week-old C57BL/6 mouse brains were isolated and homogenized by sonication in 10 mM HEPES, 5 mM EDTA, 0.3 M sucrose, and protease inhibitors. The homogenate was layered on a sucrose gradient of 0.32 M and 0.85 M sucrose in 10 mM HEPES, 5 mM EDTA (pH 7.4) and centrifuged at 75,000*g* for 30 minutes with a SW41 Ti rotor (Beckman Coulter). The crude myelin fraction was carefully isolated from the interface, and subjected to three rounds of osmotic shock in ultrapure water and centrifugation at 75,000*g* for 15 min. The resulting pellet was subjected to the same procedure to obtain a pure myelin fraction. The yield of myelin was calculated by measuring the total amount of protein with the Bradford assay (Biorad, 500-0006). For the fluorescence labeling of myelin, the amount of myelin with 250 µg of protein was labeled with PKH26 (MINI26-1KT, Sigma). For the in vitro experiments, myelin was always sonicated before administration to the cells. As the particles of myelin precipitates in solution, the amount of administered myelin was calculated per surface area (10 µg of myelin per cm^2).

Immunohistochemistry

The animals were anesthetized by intraperitoneal injection of 14% chloral hydrate and transcardially perfused with 4% paraformaldehyde (PFA) with a MPII mini peristaltic pump (Harvard Apparatus) (flow rate: 3 ml/min). Brain and spinal cord tissue were postfixed overnight in 4% PFA and cryoprotected in 30% sucrose in phosphate buffer solution (PBS). The tissue was then embedded in Tissue-Tek O.C.T., and frozen on dry ice. 14 µm coronal sections were prepared using cryostat Leica CM 1900, mounted on Superfrost Plus slides and stored at -20 °C. For the staining, the sections were air dried for 1 hour at room temperature and then rinsed with 1× PBS. The sections were then blocked and permeabilized in blocking solution (2.5% bovine serum albumin, 2.5% fish gelatin and 2.5% fetal calf serum in PBS) containing 0.1% Triton X for 1 hour at room temperature. The sections were incubated overnight at 4 °C with the primary antibodies, diluted in blocking solution. The sections were washed 3 times in PBS and then incubated with secondary antibodies for 1 hour at room temperature. The sections were repeatedly washed with PBS and once in distilled water and then mounted with fluorescence mounting medium (Sigma-Aldrich, 81381). For the labeling of intracellular accumulation of myelin, the staining with Fluoromyelin was performed after the incubation with the secondary antibodies. The sections were incubated with a solution of Fluoromyelin (Thermo Fisher Scientific, F34652) (1:350) in PBS for 30 min at room temperature. The sections were then washed twice with PBS and mounted or processed for additional stainings. For the labeling of dead cells, 14 µm tissue sections from 21 dpi lesions were stained with the in situ Cell Death Detection kit (Roche, 11684795910), according to the manufacturer's instructions. For the staining with oligodendrocyte markers, antigen retrieval was performed by autoclaving the section for 20 minutes in 10 mM Sodium Citrate buffer (pH 6). The sections were then blocked in blocking solution and 0.3% Triton X-100 for one hour and with the primary antibody for 48 hours. The antibodies used were: IBA1 (Wako, 019-19741), Mac-2 (Biolegend, 125401) MHC-II (Novus Biologicals, NB100-65541), LAMP1 (lysosomal-associated membrane protein 1, Santa Cruz Biotechnology, sc-19992), APC1 (clone CC1, Abcam, ab16794), NKX 2.2 (Developmental Studies Hybridoma Bank, 74.5A5), OLIG2 (Millipore, ab 9610) and cleaved caspase 3 (Cell Signaling, 9579). Secondary antibodies: for fluorescence microscopy we used Alexa Fluor 488-, 647- and 555-conjugated antibodies (Invitrogen, A-11034, A-28175, A-21422, A-21443, A27018 and A27039, respectively). The phagocytes were also labeled with Dylight594 tomato lectin (Vector Laboratories, DL-1177) or Alexa Fluor Choleratoxin B (Thermo Scientific, C34778) for 30 min at room temperature in PBS. For the luxol fast blue (LFB) staining, the sections

were air dried and passed through increasing concentrations of ethanol in distilled water (50%, 75%, 90% and 100%), the sections were then incubated in the luxol fast blue solution (0.1% LFB in 95% ethanol and 0.05% glacial acetic acid) at 60 °C overnight. The sections were washed with 96% ethanol, distilled water and, briefly in 0.05% lithium carbonate. The non-specific staining was cleared in 70% ethanol until only the white matter was visible. The sections were then mounted with Depex. For the counting of cells per mm^2, each section was stained for the specific markers, and the adjacent section was stained with Luxol fast blue to identify the borders of the lesions.

To measure the lesion volume, the area of demyelination shown by negative Fluoromyelin staining was measured in consecutive sections of a lesion which were separated by a known distance. Lesion volume was calculated according to the truncated cone model using the formula:

$$V = \sum_{i=1}^{n-1} \frac{1}{3}\pi(r_i^2 + r_{i+1}^2 + r_i r_{i+1})d$$

Where n is the number of sections, r the radius of lesion area and d the distance of consecutive sections. Lesion areas were measured using ImageJ software and analyzed in an automated fashion using IPython.

Caspase-1 activity was determined with the FAM FLICA Caspase-1 assay (ImmunoChemistry Technologies). Spinal cords were isolated and directly frozen in Tissue Tek. The tissues were then cut in 14 µm sections, which were then left to dry for 30 min at 37°C. The sections were fixed in acetone for 1 minute, rehydrated in TBS-Tween-20 and blocked for 30 min in blocking solution. The sections were then incubated with the caspase 1 specific FAM-YVAD-FMK reagent (150X, further diluted 1:50) for 1 hour, washed in TBS-Tween 20 and then counterstained with DAPI. The sections were finally mounted with MOWIOL and imaged.

Cell culture

For the preparation of bone marrow derived macrophages (BMDM), the femur and tibia of 8 weeks old C57BL/6 mice were isolated and cut at the extremities. The bone marrow was flushed out with DMEM, resuspended to a single-cell suspension by repeated pipetting and passed through a cell strainer. The cells were then plated in culture media (DMEM supplemented with 10% fetal calf serum, 1% penicillin/streptomycin, and 1% glutamate) with

20% of MCSF-enriched cell culture supernatant from the L929-cell line for at least 7 days. Microglia from mouse brain was prepared as previously described (*24*). Briefly, mixed glia culture was obtained from a P1 mouse brain and cultured in DMEM supplemented with 10% fetal calf serum, 20% L929-conditioned media, 1% penicillin/streptomycin, and 1% glutamate. Microglia was shaken off and plated for the experiment. For the myelin treatment, the cells were washed twice and incubated with purified myelin in serum free media to remove the effect of the serum lipoproteins. Two hours after the initial administration, the cells were washed and left for the experiment time. The compounds used were: caspase 1 inhibitor z-YVAD-fmk (10 µM, 1012-100, Biovision), cathepsin B inhibitor CA074me (10 µM, 205531, EMD Millipore), staurosporine (1 µM Sigma, S5921-1MG), GW3965 (1 µM Selleckchem, S2630). The APOE mimetic peptide ATI-5261 (EVRSKLEEWFAAFREFAEEFLARLKS) was synthesized by JT Peptide (concentration in vitro 30µg/ml). The amount of intracellular myelin particles was determined by staining of myelin treated microglial cultures with FluoroMyelin. The area of FluoroMyelin-positive particles was measured for each position of the coverslip and divided by the cell number as determined by DAPI staining to obtain myelin particle area per cell. Between 150 and 450 cells were analyzed per experiment.. Astrocytic cultures were prepared by shaking off microglia cells from mixed glial cultures. To obtain astrocyte conditioned media, astrocytic cultures were washed twice with PBS and subsequently grown in cell culture media (DMEM supplemented with 1% lipid free BSA, 1% penicillin/streptomycin, and 1% glutamate) for one day. Media was taken off and centrifuged at 5000g to remove cells. For the isolation of inflammatory cells from the brain of the ABCA1/G1 KO mice, the brain were isolated and reduced to a single cell suspension with the Adult Brain Dissociation Kit (Miltenyi, 130-107-677), according to the manufacturer's protocol. The cells were then incubated with anti CD11b beads, pelleted and processed for RNA isolation.

Imaging of cholesterol crystals

For the visualization of crystals, 14 µm tissue sections and fixed cells were labeled with Dylight-594-conjugated GSL I-B_4 isolectin (Vector Laboratories, DL1207) or Alexa Fluor 647-conjugated choleratoxin B (Thermoscientific, C34778) and DAPI. The sections were then imaged in a Leica SP2 AOBS confocal microscope, where the stainings were imaged with regular confocal settings, while the crystals were imaged as previously described (*14*). For the quantification of the crystals, at least two random 100x pictures per lesion were taken from three lesions per group. The integrated density area was calculated and every 10^6 units

were converted in one arbitrary unit. For the quantification of crystals in vitro, the integrated density area per cell was calculated with CellProfiler (http://cellprofiler.org). The area of the cell was identified by labeling of the cell with fluorescently labeled lectin or cholera toxin. Between 30 and 350 cells were measured per group.

Cholesterol crystal preparation

Cholesterol crystals were prepared as previously described (*25*). Briefly, cholesterol (Sigma, C8667-5G) was dissolved in 50 ml of 1- Propanol and distilled water (1:1.5). 1-Propanol was removed by evaporation and the crystals were resuspended in PBS with 0.05% BSA.

Subcellular fractionation and cathepsin B activity assay

For subcellular fractionation, the cytosol and membrane fractions were prepared as previously described (*26*). Briefly, the cells were washed twice in PBS and incubated with MSH-Buffer (210 mM mannitol, 70 mM sucrose, 20 mM HEPES pH 7.5, 1 mM EDTA, 300 μM Pefabloc, 100 μM PMSF) for 45 min on ice. Cells were then scraped and lysed with 10 passages through a 25-G needle. Cells were then centrifuged for 5 min at 350 g to pellet and remove cellular debris and the nuclei. The supernatant was further centrifuged for 100 000 g for 45 min to obtain the cytosol. The pellet (membrane fraction), was resuspended in a buffer containing 200 mM NaOAc, 1 mM EDTA, 0.1% Brij 35, 0.1% Triton X-100 at pH 6.7. 40 µg of proteins per fraction were mixed in assay buffer to a final volume of 95 µl and 5 µl of Z-Arg-Arg-7-amido-4-methylcoumarin (Arg-Arg-7AMC, Sigma-Aldrich, C5429) and incubated for 60 min at 37°C. The fluorescent emission at 440 nm resulting upon 348 nm excitation was compared to a standard curve of 7AMC and the result expressed in nmol of 7AMC released per mg of protein per minute.

RNA isolation and gene expression analysis

For the preparation of RNA from lesions, the animals were sacrificed and the freshly injected tissue was carefully isolated. The fresh tissue was embedded in 20% gelatin and 200 µm sections were prepared with a vibratome. The lesions was identified by the presence of Monastral blue, isolated and frozen in liquid nitrogen. The samples were homogenized in TRIZOL (Sigma, 93289-100ML) with a Polytron, and chloroform was added. After centrifugation, the aqueous phase was transferred to a new tube and the RNA was isolated with the RNAeasy isolation kit (Qiagen, 74104). The RNA was retrotranscribed with the Superscript III kit (Thermo Fisher Scientific, 18080051) and the

quantitative PCR was performed with the Power SYBR green PCR Master mix (4367659 Thermo Fisher Scientific). For the isolation of RNA from cells, the cells were collected in TRIZOL and processed as described above. The relative quantification of each gene was performed with the ΔΔCt method. The following primers were used: ApoE forward, 5'-ctgacaggatgcctagcc; ApoE reverse 5'-tcccagggttggttgctttg; Abca1 forward 5'-tgtctgaaaaaggaggacagtg; Abca1 reverse 5'-tgtcactttcatggtcgctg; Abcg1 forward 5'-cagacgagagatggtcaaaga; Abcg1 reverse 5'-tcaaagaacatgacaggcgg; RPLP0 forward 5'-aaactgctgcctcacatccg; RPLP0 reverse 5'- agcagctggcaccttattgg; Cyp46a1 forward 5'-ttggggagagactgtttggc; Cyp46a1 reverse 5'-tcgttgaacgtctccatcagg; Cyp27a1 forward 5'-gaatctggctagtgccccac; Cyp27a1 reverse 5'-cattgctctccttgtgcgatg.

Western blot analysis

Cells were collected and resuspended in RIPA buffer (150 mM NaCl, 1.0% Triton-X100, 0.5% sodium deoxycholate, 0.1% SDS, 50 mM Tris, pH 8.0). Cell lysates were cleared of cellular debris by centrifugation (13000 rpm for 10 minutes) and equal amounts of protein were separated by SDS-PAGE on 12% gels and transferred to nitrocellulose membranes. The membranes were blocked (3% milk, 1% BSA in PBS and 0.05% Tween 20), incubated with primary antibodies overnight in blocking solution and washed with PBST three times. The membranes were then incubated with horseradish peroxidase–conjugated secondary antibodies for 1 hour at room temperature. After washing in PBST, the membranes were visualized using an enhanced chemiluminescence system (Pierce, Cat.N.32106). The antibodies used were: anti p20 subunit of caspase 1 (Abcam, ab17820), anti cathepsin B (R&D System, AF965), anti γ-Tubulin (Sigma-Aldrich, T6557).

Acridine Orange staining

AO is a lipophilic dye that freely diffuses inside the cell. Inside the lysosomes, AO is protonated and sequestered, shifting its emission towards the red channel. Upon breakdown of the lysosomal membrane and subsequent loss of lysosomal pH, AO shifts emission towards the green channel. To measure lysosomal permeability, the cells were incubated with 10 μM acridine orange (AO) for 15 minutes at 37°C. The fluorescence in the green and red channels was measured in random 40X fields on a Leica DMI6000 inverted microscope and the ratio between the intensities was calculated.

Enzyme-linked immunosorbent assay (ELISA)

ELISA for IL1β was purchased from Peprotech (900-K47) and performed according to the manufacturer's instructions.

Cell death quantification

At the end of the incubation with myelin, the media was removed and replaced with fresh media containing 5 µg/ml of propidium iodide (Sigma, P4170-10MG) and 5 µg/ml of Hoechst (Life Technologies, H3570) for 20 minutes. The cells were then imaged on a Leica DMI6000 inverted microscope. The number of dead cells was calculated as percentage of propidium iodide positive cells.

Caspase 1 detection

The activity of caspase 1 was measured with the Caspase-1/ICE Colorimetric Assay Kit (Biovision, K111-100), according to the manufacturer's instructions. Briefly, myelin was added to the cells for 4 hours to allow for the phagocytosis of the myelin particles, and then the cells were washed twice in fresh media. After 20 hours, the media was collected and the cells were incubated with 10 mM EDTA in PBS. After detachment, the cells were collected by centrifugation (1200 rpm, 10 min) and resuspended in lysis buffer. After 10 minutes of incubation on ice, the cells were centrifuged (10000g for 2 minutes) and the total amount of protein of the supernatant was quantified. 80 µg of protein was incubated with the reaction buffer and the YVAD-pNA substrate and the samples were left for 2 hours at 37°C. The absorbance was measured at 405 nm. For the measurement of caspase 1 activity in the lesions, the spinal cord was freshly isolated and mounted on 20% gelatin. 200-µm-thick vibratome sections were prepared and the lesion areas (identified by the presence of monastral blue) were dissected and snap-frozen in liquid nitrogen. The samples were then briefly sonicated in lysis buffer and 80 µg of proteins were taken for the activity assay.

Electron microscopy

The spinal cord was freshly isolated, embedded in 20% gelatin and sectioned into 200 µm thick vibratome sections (*27*). The sections with the lesion (recognized by the presence of the monastral blue) were immersed in fixative (4% paraformaldehyde and 2.5% glutaraldehyde in 0.1 M phosphate buffer containing 0.5% NaCl). The brain was fixed by transcardial perfusion. The brain was isolated and post-fixed in fixative solution overnight. The tissue was then sectioned into 200 µm thick vibratome sections to identify the lesion site. The sections were then postfixed in a solution of 1% osmium tetroxide in 0.1 M phosphate buffer (pH 7.4) for 30

min at room temperature. Following washing with distilled water the sections were stained with 0.5% uranyl acetate in 70% ethanol for 1 hour, dehydrated in a serial dilution of ethanol, and cleared in propylene oxide, embedded in Epon, and incubated at 60°C for 24 hours. The tissues in Epon blocks were then trimmed and reoriented so that ultrathin (60 nm) cross-sections of the lesion could be cut using the ultramicrotome. Ultrathin sections were collected on formvar-coated copper grids. For the quantification of the crystals by TEM, the crystals from at least 4 fields per lesion from three animals per group were counted. For quantification of foam cells semithin sections (500nm) on objective slides were stained with methylene blue and azur II followed by counting of foam cells in the lesion area.

Quantification of oxysterols

Sterols and oxysterols were extracted from isolated lesions by chloroform/methanol (1/1;v/v), dried under nitrogen and the residuals sterols/oxysterols were silylated to their corresponding trimethylsilylethers. The phytosterols campesterol and sitosterol, were determined by GC-mass spectrometry- selected ion monitoring, using epicoprostanol as internal standard. Cholesterol precursors such as lathosterol, lanosterol, dihydro-lanosterol, and desmosterol, together with the cholesterol metabolite 5a-cholestanol and the phytosterols, campesterol and sitosterol, were determined by GC mass spectrometry selected ion monitoring (GC-MS-SIM), using epicoprostanol as internal standard. 24S- and 27-hydroxycholesterol were measured by isotope dilution mass spectrometry (*28*) (*29*). Data are given as amount of oxysterol/campesterol per whole sample volume. The phytosterol, campesterol was used as a reference, as it is not synthesized in the human body.

Statistics

Statistical analysis was performed with GraphPad Prism (GraphPad Software, Inc.). The number of animals and culture used for the experiments are indicated in the bars graphs of the figures or in the figure legends. No statistical methods were used to predetermine sample sizes, but our sample sizes are similar to those generally employed in the field. Data distribution was assumed to be normal, but this was not formally tested. To compare two groups, a two-tailed Student's *t*-test was applied. One-way ANOVA followed by Tukey's post hoc test was performed for comparison of more than two groups. To compare the interactions between different animal or cell lines, two-way ANOVA followed by Tukey's post hoc test was used. A P-value of <0.05 was considered significant in all tests. All values are represented as mean ± SEM.

Supplemental Figures

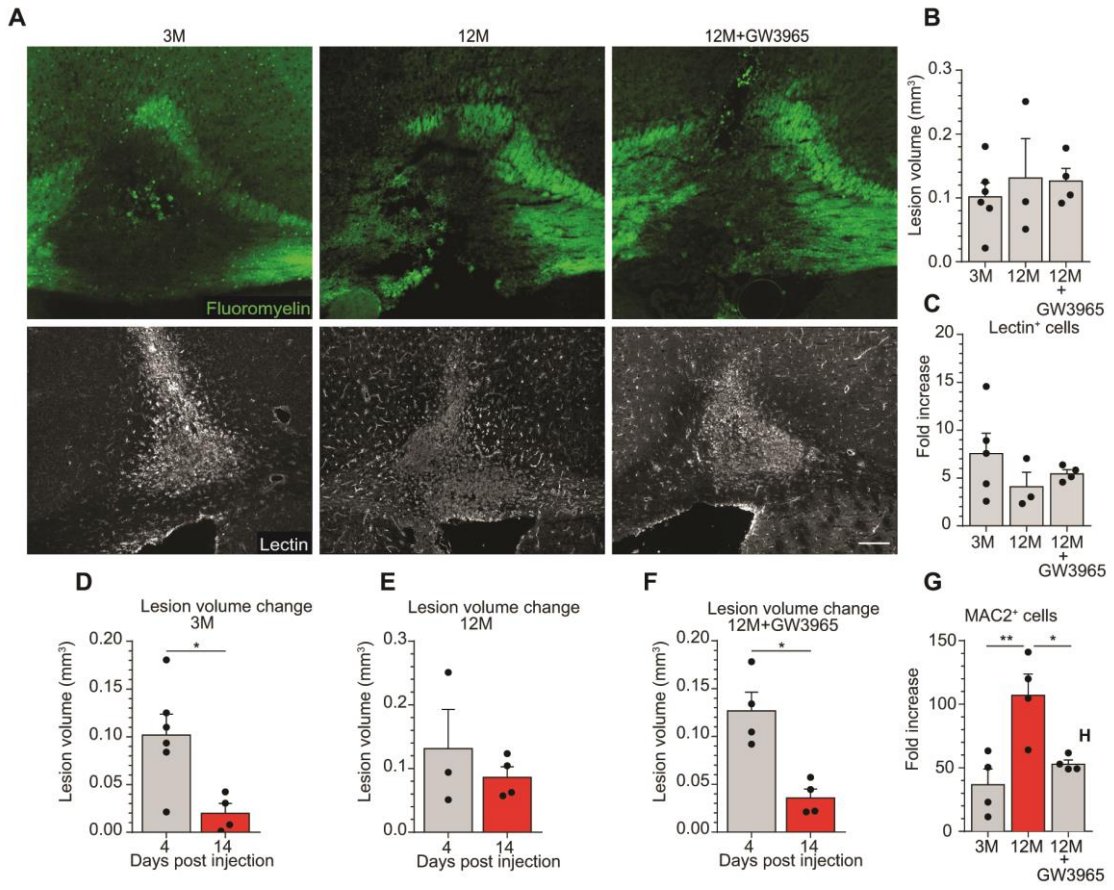

Fig. S1. Characterization of aged mice treated with GW3965.

(**A**) Images of corpus callosum lesions in 3 months (3M), 12 months (12M) and 12 months old mice treated with GW3965 (12M+GW3965) with fluoromyelin staining (green) and tomato lectin (gray) at 4 dpi. (**B**) Lesion volume in mm^3 calculated according to analysis of fluoromyelin staining of consecutive sections in 3M, untreated 12M and treated 12M+GW3965 wild-type animals at 4 dpi. (**C**) Change in number of $lectin^+$ cells in lesions as compared to contralateral unlesioned side. (**D, E, F**) Lesion volume change in 3M, untreated 12M and treated 12M+GW3965 wild-type animals at 14 dpi. (**G**) Change in $MAC2^+$ cells in 14 dpi lesions oc the corpus callosum compared to contralateral unlesioned site. All data are mean ± SEM; *P<0.05, **P<0.01, two-tailed Student´s *t*-test Scale bar, 200 µm.

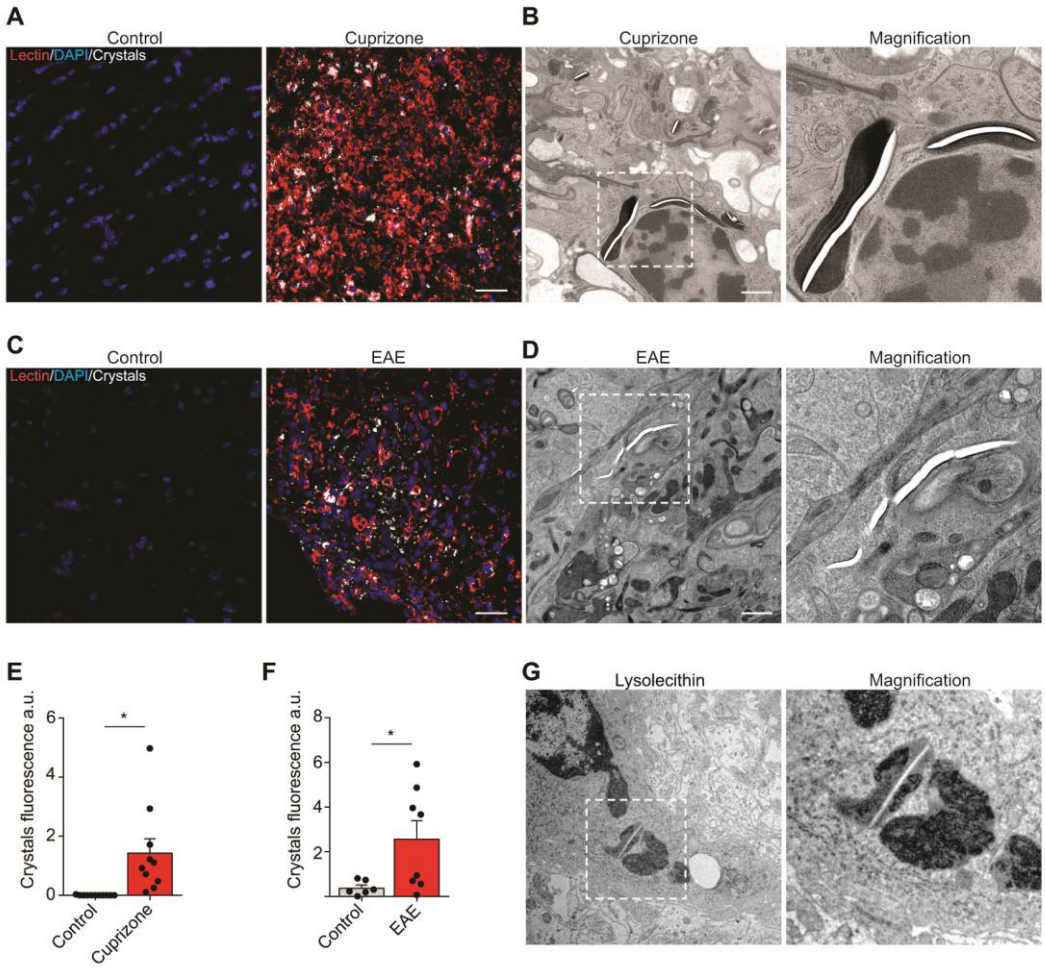

Fig. S2. Crystal formation in demyelinating lesions

(**A**) Reflection microscopy images with crystals (white) and lectin^{+} phagocytes (red). (**B**) Transmission electron micrographs of a foam cell containing lysosomal crystals in the corpus callosum of cuprizone fed mice. Boxed area shown at higher magnification. (**C**) Reflection microscopy images with crystals (white) and lectin^{+} phagocytes (red). (**D**) Transmission electron micrographs of a foam cell containing lysosomal crystals in Biozzi experimental autoimmune encephalomyelitis. Boxed area shown at higher magnification. (**E**) Relative quantification of crystals in mice fed with regular or cuprizone containing diet for 4 weeks and (**F**) relative quantification of crystals in spinal cord demyelinating lesions of Biozzi ABH mice with experimental autoimmune encephalomyelitis. (**G**) Transmission electron micrographs of a foam cell containing lysosomal crystals in a lysolecithin-induced corpus callosum lesion of a 12 month-old mouse. Boxed area shown at higher magnification. All data are mean ± SEM; *P<0.05, two-tailed Student´s *t*-test. Scale bar, 20 µm (A, B), 1 µm (B, D).

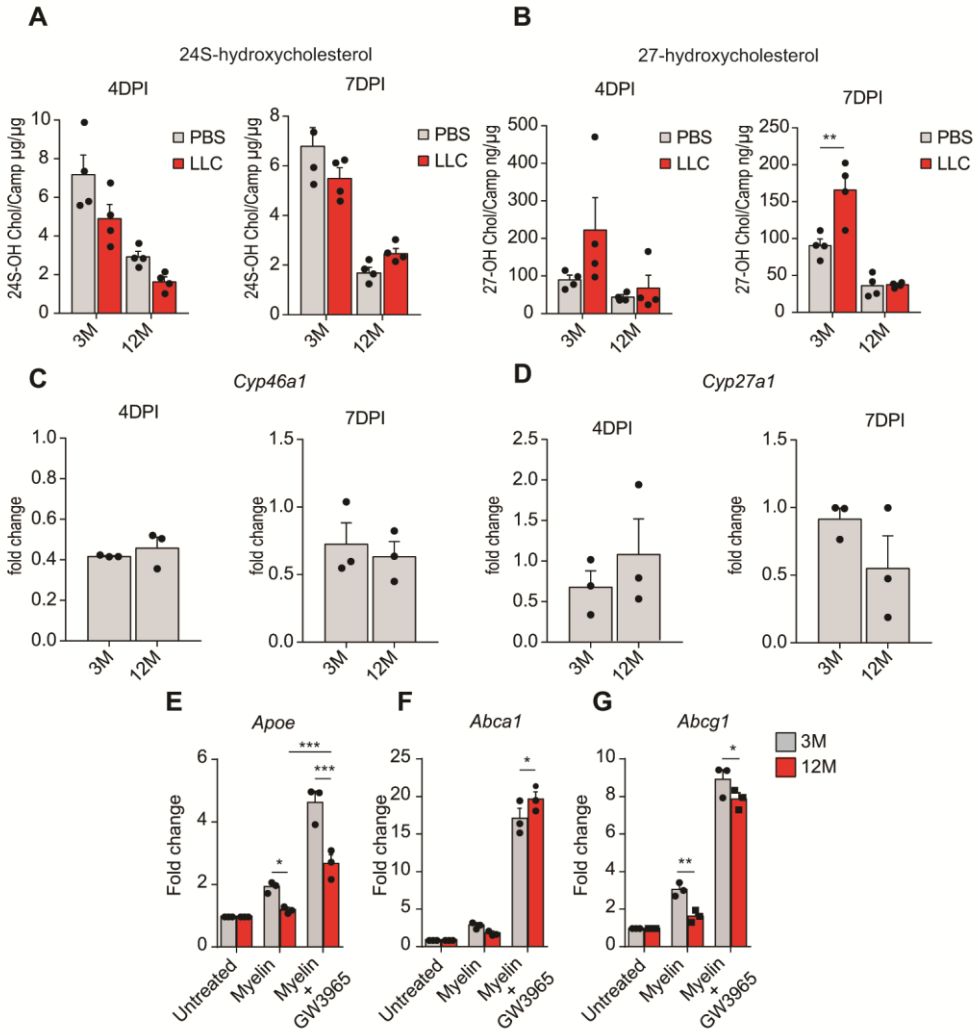

Fig. S3. Impaired upregulation of genes and metabolites associated with reverse cholesterol transport in aged phagocytes.

(**A, B**) Gas chromatography-mass spectrometry analysis of 24S-hydroxycholesterol and 27-hydroxycholesterol 4 and 7 dpi lesions of the corpus callosum. Each cholesterol species was normalized to the amount of campesterol and compared to the PBS-injected corpus callosum. Gene expression analysis using qPCR for (**C**) *Cyp46a1*and (**D**) *Cyp27a1* in 4 and 7 dpi lesions of the corpus callosum. Data are expressed as fold change compared to the contralateral, PBS injected lesions. Gene expression analysis using qPCR for (**E**) *Apoe*, (**F**) *Abca1* and (**G**) *Abcg1* in BMDM isolated from 3M or 12M old mice. Myelin debris treatment was for 24 h. GW3965 was added one hour before treatment with myelin debris. *P<0.05; **P<0.01, ***P<0.001 by two way ANOVA test with Tukey's multiple comparison test.

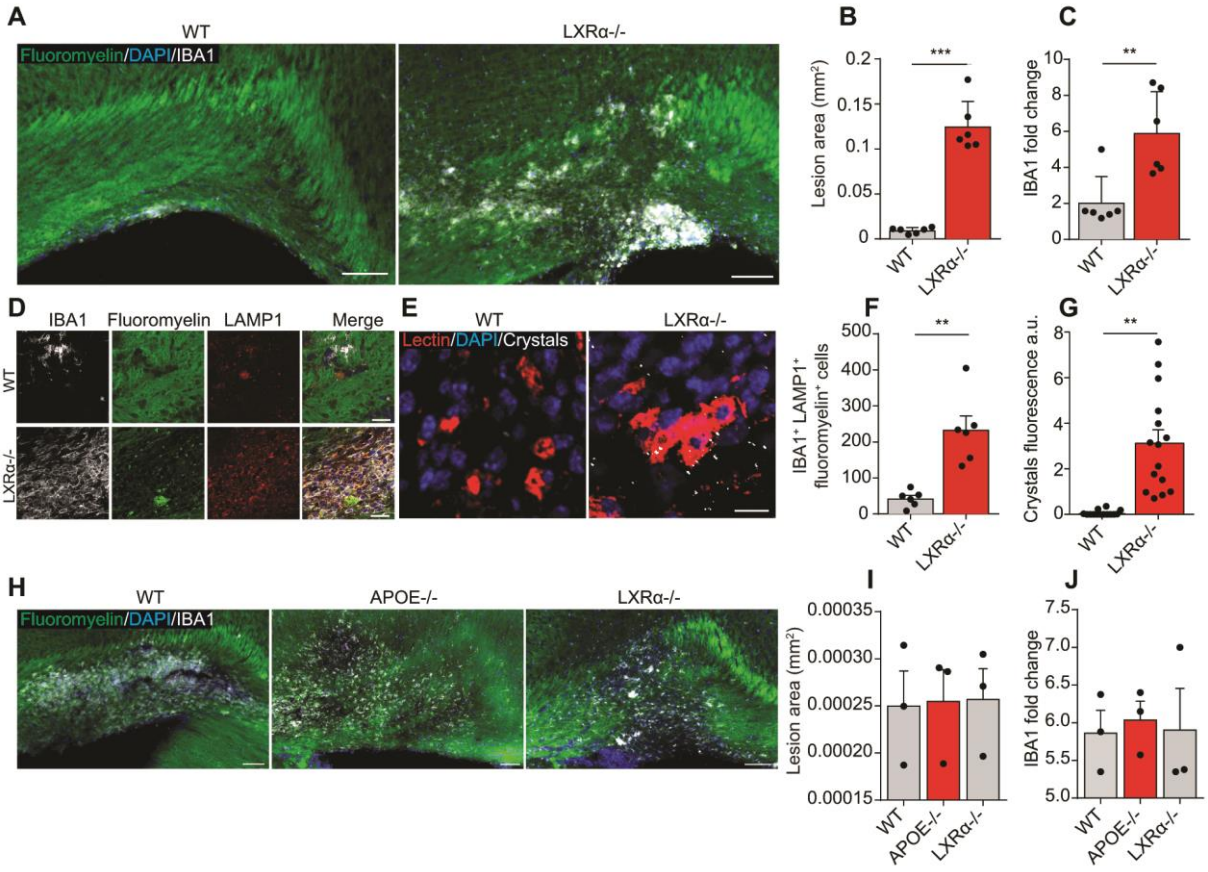

Fig. S4. Impaired lesion recovery and crystal formation in LXRα-/- mice.

(**A**) Images of corpus callosum lesions in WT and LXRα-/- mice showing fluoromyelin staining (green), IBA1 (white) and DAPI (blue) at 21 dpi. Scale bar, 100µm. (**B**) Quantification of lesion area in mm^2 by fluoromyelin staining in WT and LXRα-/- mice at 21 dpi. ***P<0.001, two-tailed Student´s *t*-test. (**C**) Change in the number of $IBA1^+$ cells in lesions as compared to contralateral unlesioned side. ** P<0.01, two-tailed Student´s *t*-test. (**D**) Confocal images of corpus callosum lesions in WT and LXRα-/- mice showing $IBA1^+$ cells (white), fluoromyelin (green) and LAMP1 (red) at 21 dpi. Scale bar, 25µm. (**E**) Reflection microscopy images of lysolecithin lesions with crystals (white), $lectin^+$ phagocytes (red) and DAPI (blue) at 21 dpi. Scale bar, 100 µm. (**F**) Number of $IBA1^+$/$fluoromyelin^+$/$LAMP1^+$ cells per mm^2 in lesioned corpus callosum at 21 dpi. ***P<0.001, two-tailed Student´s *t*-test. (**G**) Quantification of crystals in lysolecithin lesions of WT mice and LXRα-/- mice at 14 dpi. (**H**) Immunostaining of corpus callosum lesions in WT, APOE-/- and LXRα-/- mice showing fluoromyelin staining (green), IBA1 (white) and DAPI (blue) at 4 dpi. (**I**) Quantification of lesion area in mm^2 in WT, APOE-/-, LXRα-/- as

determined by fluoromyelin staining at 4 dpi. (**J**) Change in number of IBA1$^+$ cells in lesions compared to contralateral unlesioned side. All data are mean ± SEM.

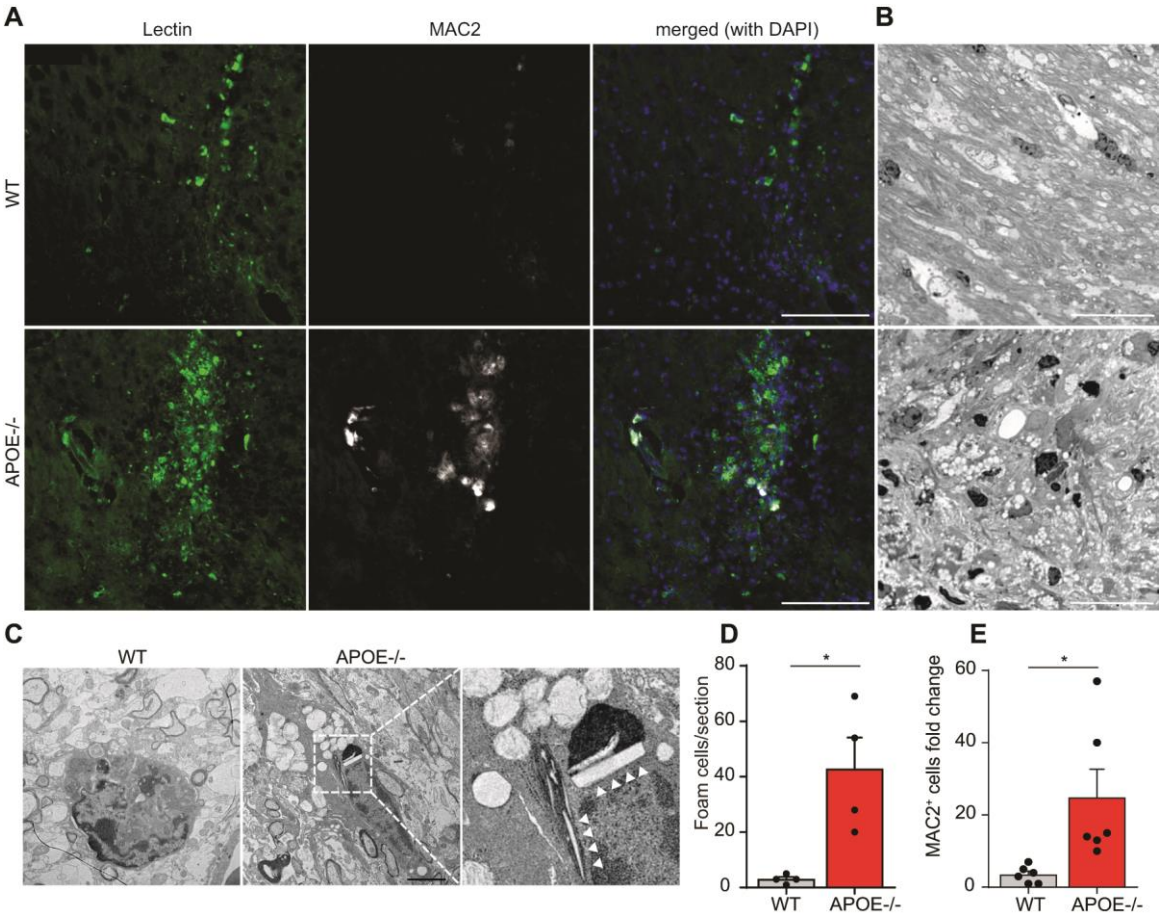

Fig. S5. Characterization of lesions in APOE-/- mice.

(**A**) Immunostaining of corpus callosum lesions in WT and APOE-/- mice showing lectin (green), MAC2 (white) and DAPI (blue) at 21 dpi Scale bar, 100 µm. (**B**) Methylenblue-Azur II staining of WT and APOE-/- lesions. Scale bar, 25µm. (**C**) Transmission electron microscopy images of foam cells in corpus callosum lesions of WT and APOE-/- mice, showing cholesterol crystals (white arrowheads) in the APOE-/- cells. Scale bar, 2.5 µm. (**D**) Relative quantification of foam cells; and (**E**) change in number of MAC2$^+$ cells in lesion as compared to contralateral unlesioned side. *P<0.05, two-tailed Student´s *t*-test.

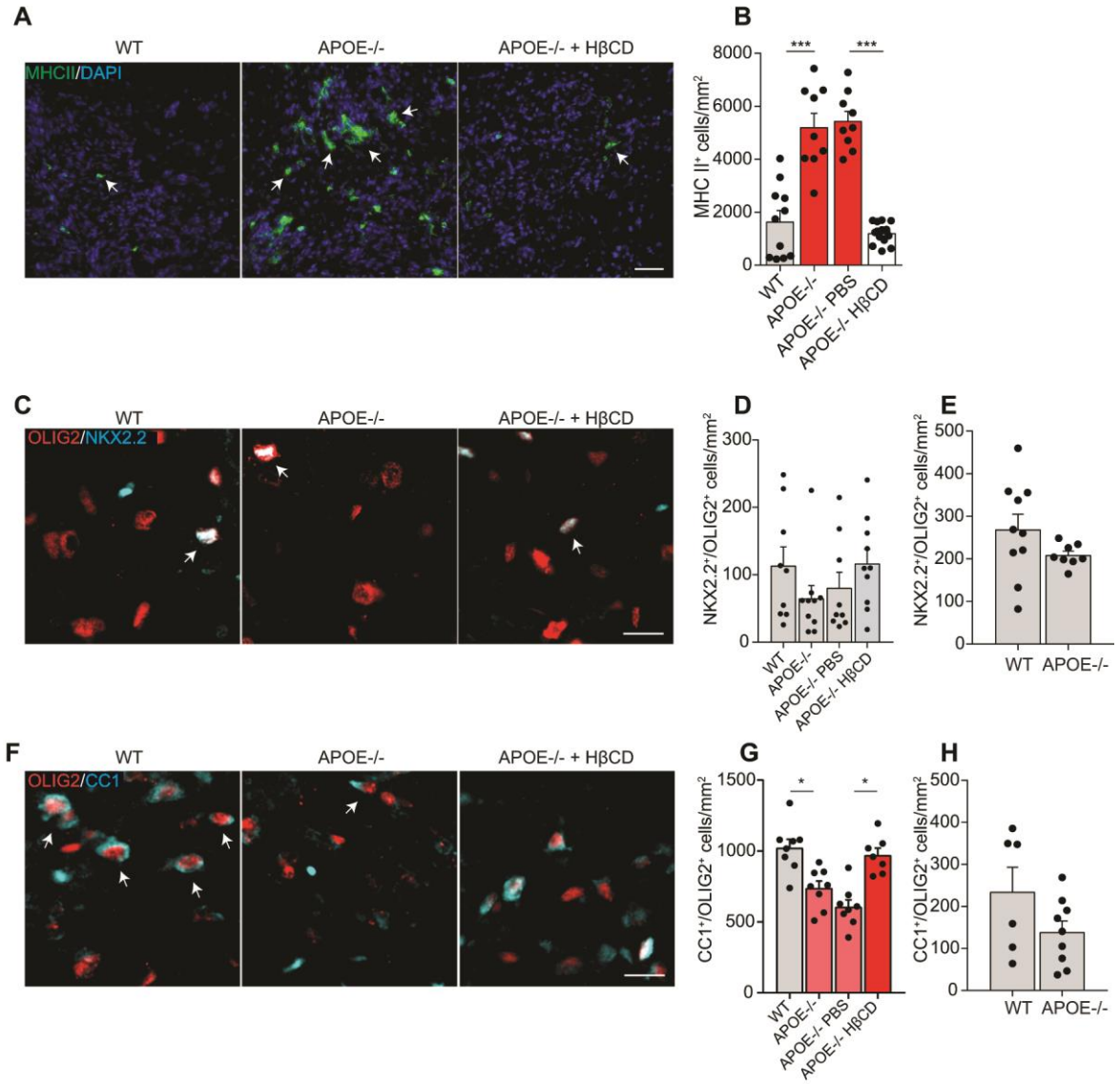

Fig. S6. Analysis of oligodendrocyte differentiation in lesions of APOE KO mice.

(**A**) Images and (**B**) relative quantification of inflammatory cells in 21 dpi lesions, identified by immunolabeling for MHC II (green). Arrows mark double positive cells. (**C**) Representative images and (**D**) relative quantification of the number of oligodendrocyte progenitor (OPC) marker using antibodies against NKX2.2 (red) and the oligodendrocyte lineage marker OLIG2 (green) in 21 dpi spinal cord lesions of wild-type (WT), APOE -/- and APOE -/- mice treated with HβCD or PBS. Arrows mark double positive cells. (**E**) Quantification of the number of OPCs in 4 dpi spinal cord lesions of WT and APOE -/- mice. (**F**) Representative images and (**G**) relative quantification of the number of mature oligodendrocytes (OL) using antibodies against APC (CC1, red) an OLIG2 (green) in 21 dpi

spinal cord lesions of WT, APOE -/- and APOE -/- mice treated with HβCD or PBS. Arrows mark double positive cells. (**H**) Quantification of the number of OLs in 4 dpi spinal cord lesions of WT and APOE -/- mice. All data are mean ± SEM; *P<0.05, by one way ANOVA test, with Tukey's multiple comparison test. Scale bar is 100 µm (A), and 25 µm (C and F).

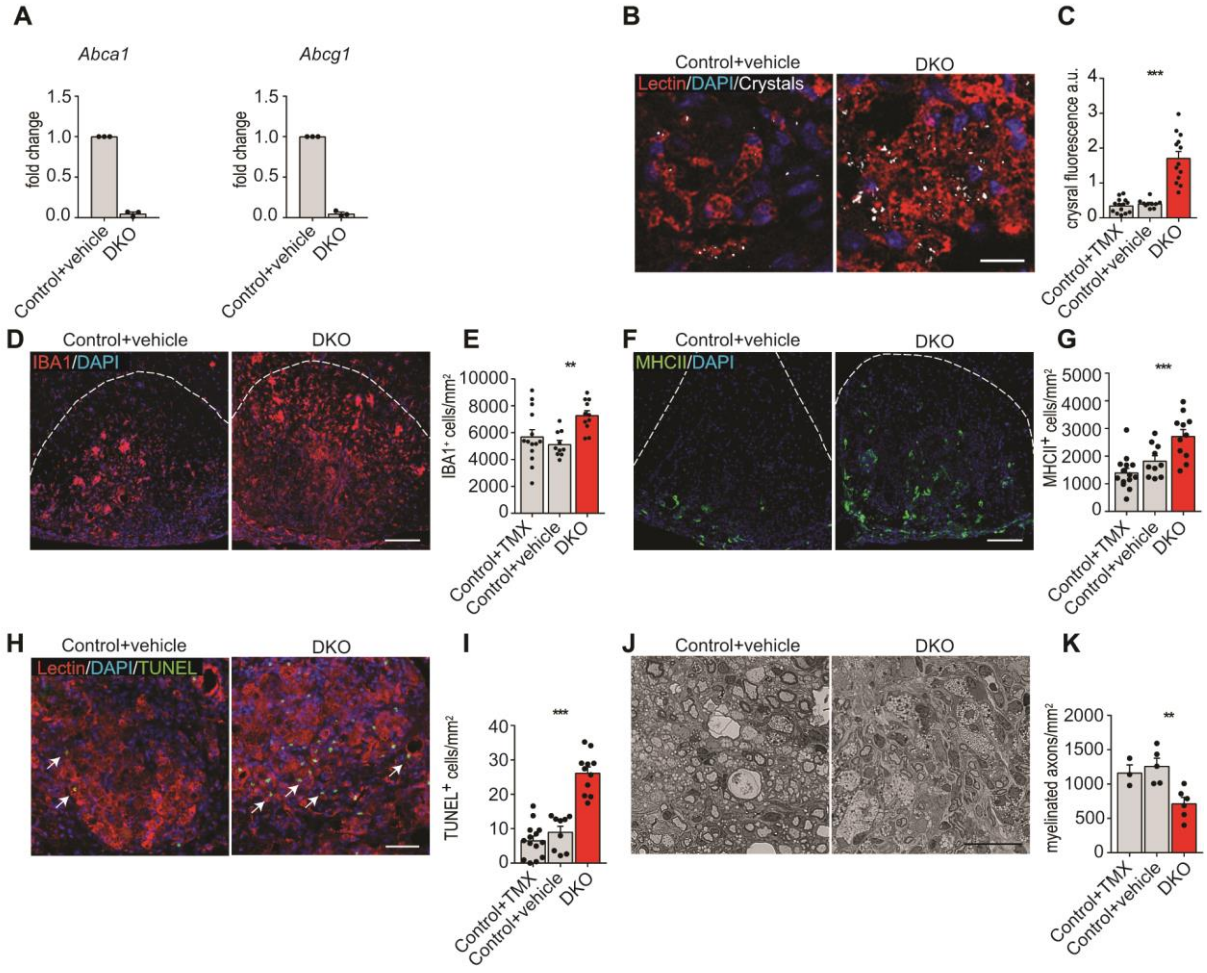

Fig. S7. Reduced remyelination, increased inflammation and crystal formation in ABCA1/G1 KO mice.

(**A**) Gene expression analysis of *Abca1* and *Abcg1* using qPCR analysis of purified microglia isolated from ABCA1/G1 KO (DKO) mice 7 days after tamoxifen treatment. Data are expressed as fold changed toward the microglia isolated from control mice. (**B**) Reflection microscopy images and (**C**) quantification of crystals (white) in lectin^{+} phagocytes (red) in 21 dpi lysolecithin lesions of ABCA1/G1 KO and control mice. (**D**) Representative images of 21

dpi lysolecithin lesions stained for IBA1 (quantification in **E**) and for MHCII (**F**, and quantification in **G**). Dashed lines indicate lesion border. (**H**) Representative images of 21 dpi lysolecithin lesions using TUNEL and lectin staining (quantification in **I**). (**J**) Representative images of semithin sections labeled with Methylenblue-Azur II in 21 dpi lesions of ABCA1/G1 KO and control mice (quantification in **K**). As control animals we used tamoxifen injected CX3CR1$^{CreERT/wt}$:Abca1$^{wt/wt}$:Abcg1$^{wt/wt}$ (Control + TMX) and vehicle (corn oil) injected CX3CR1$^{CreERT/wt}$:Abca1$^{fl/fl}$:Abcg1$^{fl/fl}$ mice (Control + vehicle). All data are mean ± SEM; for the qPCR, ***P<0.01 by two-tailed Student´s t-test. For the stainings, *P<0.05, **P<0.01, ***P<0.001 by one way ANOVA test, with Tukey's multiple comparison test. Scale bars, 10 µm (B), 100 µm (D and E), 50 µm (H) and 25 µm (J).

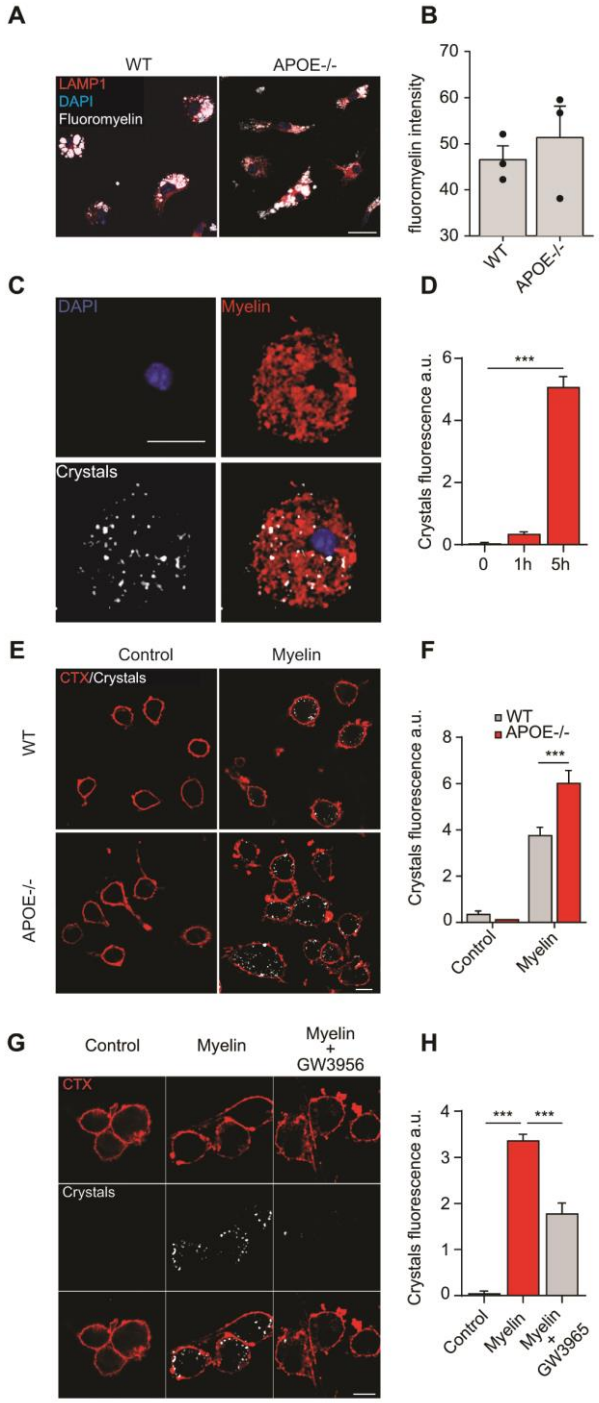

Fig. S8. Crystal formation after myelin debris overload in APOE-/- phagocytes.

(**A**) Confocal images and (**B**) relative quantification of myelin debris uptake in WT and APOE-/- cells after 4 h of treatment. The cells are labeled with fluoromyelin (white), LAMP1 (red) and DAPI (blue). Scale bar 25 µm. (**C**) Confocal images of macrophages treated with PKH26-labeled myelin (red) for 5 h, showing several crystals by reflection microscopy, and (**D**) quantification of the crystals in cells treated with myelin for 0h, 1h and 5h. (**E**) Reflection

microscopy images of WT and APOE-/- cells after 5 h of myelin debris treatment, showing the formation of crystals (white) after the incubation with myelin debris. The cell membrane is labeled with Alexa Four 647-conjugated choleratoxin B (CTX, in red). (**F**) Relative quantification of crystals by reflection microscopy. (**G**) Reflection microscopy images and (**H**) relative quantification of crystals (white) in cells incubated with myelin debris for 6 h with or without incubation with the LXR agonist GW3965 (10 µM; the agonist was added 60 min before myelin administration). For all cell culture experiments three independent cultures (n=3) with 60 to 350 cells per condition were analyzed. All data are mean ± SEM; *P<0.05, **P<0.01, ***P<0.001 by one way ANOVA test, with Tukey's multiple comparison test. Scale bars, 10 µm.

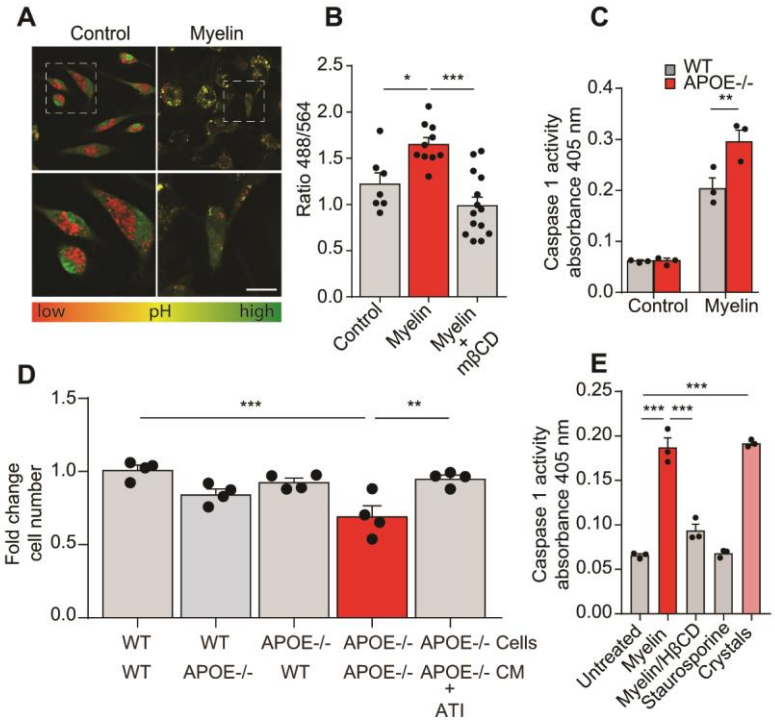

Fig. S9. Lysosomal damage and caspase1 activation after myelin debris treatment.

(**A**) Images of BMDM treated with or without myelin debris for 12 h and stained with acridine orange to depict the acidic compartment (lysosomes in red). Scale bar, 10 µm. (**B**) quantification of 488 and 594 nm fluorescence intensity ratio for each treatment. Myelin was depleted of cholesterol with mβCD before addition to BMDM (n=6 independent cultures). (**C**) Caspase 1 activity in WT and APOE-/- cells, 12 hours after myelin treatment, measured with

the colorimetric detection using YVAD-pNA as a substrate. (**D**) Microglia from WT or APOE-/- were treated with myelin and subsequently transferred in media conditioned (CM) either by WT or APOE-/- astrocytes. APOE-/- microglia cells in APOE-/- conditioned media were additionally treated with APOE mimetic peptide (ATI). Change in microglia number after myelin debris treatment as compared to untreated cells at 24 h post-treatment. (**E**) Caspase 1 activity in myelin debris treated cells, showing the increase in the protease activity in the presence of myelin debris or cholesterol crystals, but not when HβCD was administered after myelin phagocytosis. The cells were treated with staurosporine (1μM for 4 h) or cholesterol crystals (2mg/ml for 12 h) as negative and positive control, respectively. All data are mean ± SEM; *P<0.05, **P<0.01, ***P<0.001 by one way ANOVA test, with Tukey's multiple comparison test or by two way ANOVA, with Tukey's multiple comparison test.

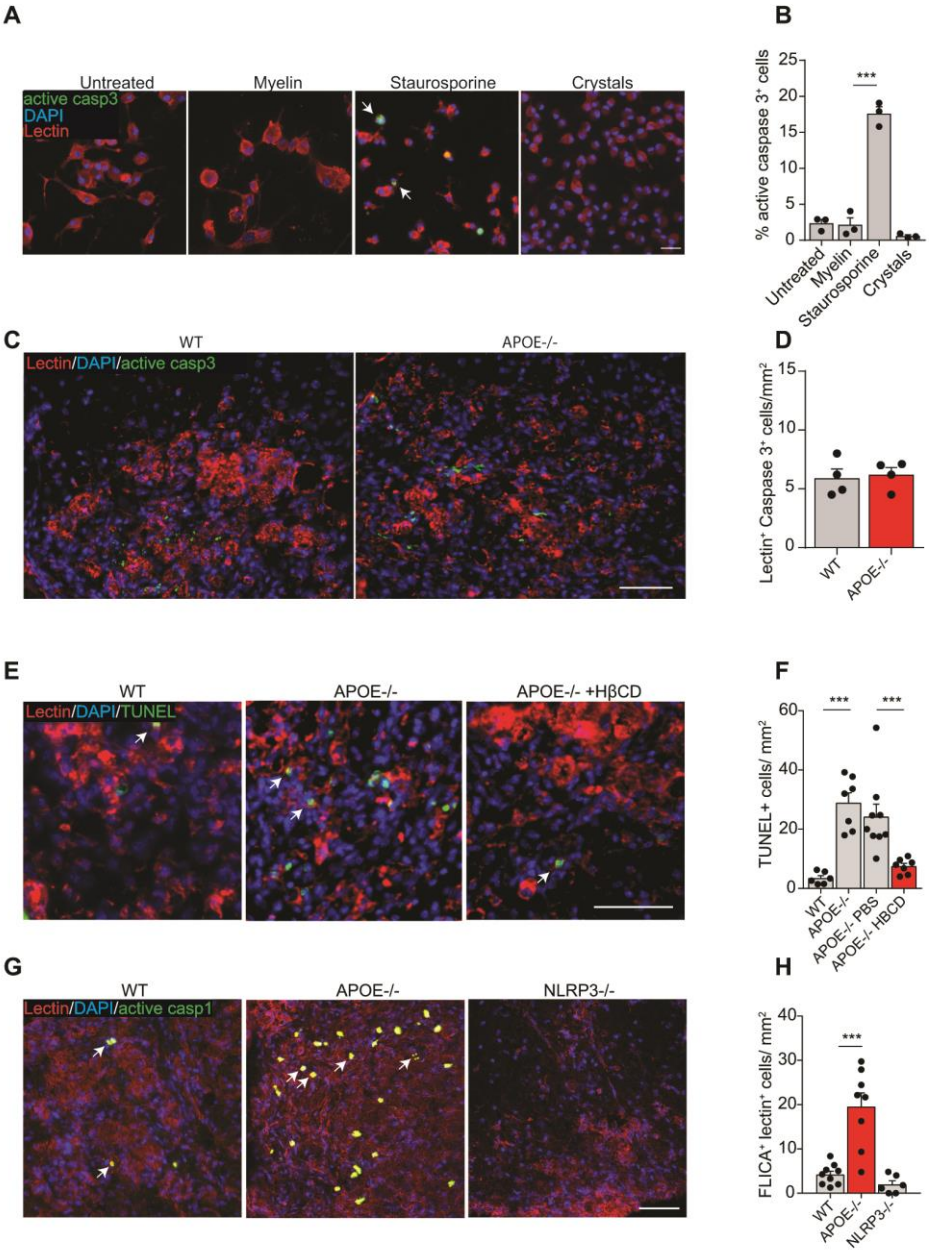

Fig. S10. Cell death after myelin debris overload is non-apoptotic.

(**A**) Immunostaining for the active fragment of caspase 3 (green, white arrowheads) and lectin (red) of cultured BMDM treated with myelin debris (15 µg/ml for 24 h), staurosporine (5 µM for 2 h) or cholesterol crystals (1 mg/ml for 4 h). (**B**) Percentage of total number of cells labeled with antibodies for the active fragment of caspase 3 (n=3 experiments with 30 cells). (**C**) Immunostaining of spinal cord lesions in WT and APOE-/- mice showing lectin (red), active caspase 3 (green) and DAPI (blue). (**D**) Quantification of lectin$^+$/active caspase 3$^+$ cells in 21 dpi lesions of WT and APOE-/- animals. (**E**) Immunostaining of spinal cord lesions in WT, APOE-/-, APOE-/- mice treated with HβCD or PBS showing lectin (red),

TUNEL (green) and DAPI (blue). (**F**) Quantification of $TUNEL^+$/$lectin^+$ cells in 21 dpi lesions. (**G**) Staining and relative quantification (**H**) for active caspase 1 (FAM-YVAD-FLICA, green), lectin (red) and nuclei (DAPI) of spinal cord lesions in WT, APOE-/- and NLRP3 mice. All data are mean ± SEM; ***P<0.001 by one way ANOVA with Tukey's multiple comparison test. Scale bars, 10 μm (A) and 50 μm (C, E and G).

References and Notes

1. P. Patrikios, C. Stadelmann, A. Kutzelnigg, H. Rauschka, M. Schmidbauer, H. Laursen, P. S. Sorensen, W. Brück, C. Lucchinetti, H. Lassmann, Remyelination is extensive in a subset of multiple sclerosis patients. *Brain* **129**, 3165–3172 (2006). doi:10.1093/brain/awl217 Medline

2. F. J. Najm, M. Madhavan, A. Zaremba, E. Shick, R. T. Karl, D. C. Factor, T. E. Miller, Z. S. Nevin, C. Kantor, A. Sargent, K. L. Quick, D. M. Schlatzer, H. Tang, R. Papoian, K. R. Brimacombe, M. Shen, M. B. Boxer, A. Jadhav, A. P. Robinson, J. R. Podojil, S. D. Miller, R. H. Miller, P. J. Tesar, Drug-based modulation of endogenous stem cells promotes functional remyelination in vivo. *Nature* **522**, 216–220 (2015). doi:10.1038/nature14335 Medline

3. F. Mei, S. P. J. Fancy, Y.-A. A. Shen, J. Niu, C. Zhao, B. Presley, E. Miao, S. Lee, S. R. Mayoral, S. A. Redmond, A. Etxeberria, L. Xiao, R. J. M. Franklin, A. Green, S. L. Hauser, J. R. Chan, Micropillar arrays as a high-throughput screening platform for therapeutics in multiple sclerosis. *Nat. Med.* **20**, 954–960 (2014). doi:10.1038/nm.3618 Medline

4. V. A. Deshmukh, V. Tardif, C. A. Lyssiotis, C. C. Green, B. Kerman, H. J. Kim, K. Padmanabhan, J. G. Swoboda, I. Ahmad, T. Kondo, F. H. Gage, A. N. Theofilopoulos, B. R. Lawson, P. G. Schultz, L. L. Lairson, A regenerative approach to the treatment of multiple sclerosis. *Nature* **502**, 327–332 (2013). doi:10.1038/nature12647 Medline

5. J. M. Ruckh, J.-W. Zhao, J. L. Shadrach, P. van Wijngaarden, T. N. Rao, A. J. Wagers, R. J. M. Franklin, Rejuvenation of regeneration in the aging central nervous system. *Cell Stem Cell* **10**, 96–103 (2012). doi:10.1016/j.stem.2011.11.019 Medline

6. S. Shen, J. Sandoval, V. A. Swiss, J. Li, J. Dupree, R. J. M. Franklin, P. Casaccia-Bonnefil, Age-dependent epigenetic control of differentiation inhibitors is critical for remyelination efficiency. *Nat. Neurosci.* **11**, 1024–1034 (2008). doi:10.1038/nn.2172 Medline

7. V. E. Miron, A. Boyd, J.-W. Zhao, T. J. Yuen, J. M. Ruckh, J. L. Shadrach, P. van Wijngaarden, A. J. Wagers, A. Williams, R. J. M. Franklin, C. Ffrench-Constant, M2 microglia and macrophages drive oligodendrocyte differentiation during CNS remyelination. *Nat. Neurosci.* **16**, 1211–1218 (2013). doi:10.1038/nn.3469 Medline

8. K. J. Moore, I. Tabas, Macrophages in the pathogenesis of atherosclerosis. *Cell* **145**, 341–355 (2011). doi:10.1016/j.cell.2011.04.005 Medline

9. X. Fu, J. G. Menke, Y. Chen, G. Zhou, K. L. MacNaul, S. D. Wright, C. P. Sparrow, E. G. Lund, 27-hydroxycholesterol is an endogenous ligand for liver X receptor in cholesterol-loaded cells. *J. Biol. Chem.* **276**, 38378–38387 (2001). doi:10.1074/jbc.M105805200 Medline

10. C. Hong, P. Tontonoz, Liver X receptors in lipid metabolism: Opportunities for drug discovery. *Nat. Rev. Drug Discov.* **13**, 433–444 (2014). doi:10.1038/nrd4280 Medline

11. R. W. Mahley, Apolipoprotein E: Cholesterol transport protein with expanding role in cell biology. *Science* **240**, 622–630 (1988). doi:10.1126/science.3283935 Medline

12. S. Zimmer, A. Grebe, S. S. Bakke, N. Bode, B. Halvorsen, T. Ulas, M. Skjelland, D. De Nardo, L. I. Labzin, A. Kerksiek, C. Hempel, M. T. Heneka, V. Hawxhurst, M. L. Fitzgerald, J. Trebicka, I. Björkhem, J.-A. Gustafsson, M. Westerterp, A. R. Tall, S. D. Wright, T. Espevik, J. L. Schultze, G. Nickenig, D. Lütjohann, E. Latz, Cyclodextrin promotes atherosclerosis regression via macrophage reprogramming. *Sci. Transl. Med.* **8**, 333ra50 (2016). doi:10.1126/scitranslmed.aad6100 Medline

13. A. Hafiane, J. K. Bielicki, J. O. Johansson, J. Genest, Apolipoprotein E derived HDL mimetic peptide ATI-5261 promotes nascent HDL formation and reverse cholesterol transport in vitro. *Biochim. Biophys. Acta* **1841** , 1498–1512 (2014). doi:10.1016/j.bbalip.2014.07.018 Medline

14. P. Duewell, H. Kono, K. J. Rayner, C. M. Sirois, G. Vladimer, F. G. Bauernfeind, G. S. Abela, L. Franchi, G. Nuñez, M. Schnurr, T. Espevik, E. Lien, K. A. Fitzgerald, K. L. Rock, K. J. Moore, S. D. Wright, V. Hornung, E. Latz, NLRP3 inflammasomes are required for atherogenesis and activated by cholesterol crystals. *Nature* **464**, 1357–1361 (2010). doi:10.1038/nature08938 Medline

15. K. Rajamäki, J. Lappalainen, K. Oörni, E. Välimäki, S. Matikainen, P. T. Kovanen, K. K. Eklund, Cholesterol crystals activate the NLRP3 inflammasome in human macrophages: A novel link between cholesterol metabolism and inflammation. *PLOS ONE* **5**, e11765 (2010). doi:10.1371/journal.pone.0011765 Medline

16. A. Aguzzi, B. A. Barres, M. L. Bennett, Microglia: Scapegoat, saboteur, or something else? *Science* **339**, 156–161 (2013). doi:10.1126/science.1227901 Medline

17. J. K. Huang, A. A. Jarjour, B. N. Oumesmar, C. Kerninon, A. Williams, W. Krezel, H. Kagechika, J. Bauer, C. Zhao, A. Baron-Van Evercooren, P. Chambon, C. Ffrench-Constant, R. J. M. Franklin, Retinoid X receptor gamma signaling accelerates CNS remyelination. *Nat. Neurosci.* **14**, 45–53 (2011). doi:10.1038/nn.2702 Medline

18. D. Meffre, G. Shackleford, M. Hichor, V. Gorgievski, E. T. Tzavara, A. Trousson, A. M. Ghoumari, C. Deboux, B. Nait Oumesmar, P. Liere, M. Schumacher, E.-E. Baulieu, F. Charbonnier, J. Grenier, C. Massaad, Liver X receptors alpha and beta promote myelination and remyelination in the cerebellum. *Proc. Natl. Acad. Sci. U.S.A.* **112**, 7587–7592 (2015). doi:10.1073/pnas.1424951112 Medline

19. F. Bei, H. H. C. Lee, X. Liu, G. Gunner, H. Jin, L. Ma, C. Wang, L. Hou, T. K. Hensch, E. Frank, J. R. Sanes, C. Chen, M. Fagiolini, Z. He, Restoration of visual function by enhancing conduction in regenerated axons. *Cell* **164**, 219–232 (2016). doi:10.1016/j.cell.2015.11.036 Medline

20. J. A. Piedrahita, S. H. Zhang, J. R. Hagaman, P. M. Oliver, N. Maeda, Generation of mice carrying a mutant apolipoprotein E gene inactivated by gene targeting in embryonic stem cells. *Proc. Natl. Acad. Sci. U.S.A.* **89**, 4471–4475 (1992). doi:10.1073/pnas.89.10.4471 Medline

21. G. Liang, J. Yang, J. D. Horton, R. E. Hammer, J. L. Goldstein, M. S. Brown, Diminished hepatic response to fasting/refeeding and liver X receptor agonists in mice with selective deficiency of sterol regulatory element-binding protein-1c. *J. Biol. Chem.* **277**, 9520–9528 (2002). doi:10.1074/jbc.M111421200 Medline

22. M. Westerterp, S. Gourion-Arsiquaud, A. J. Murphy, A. Shih, S. Cremers, R. L. Levine, A. R. Tall, L. Yvan-Charvet, Regulation of hematopoietic stem and progenitor cell mobilization by cholesterol efflux pathways. *Cell Stem Cell* **11**, 195–206 (2012). doi:10.1016/j.stem.2012.04.024 Medline

23. S. Yona, K.-W. Kim, Y. Wolf, A. Mildner, D. Varol, M. Breker, D. Strauss-Ayali, S. Viukov, M. Guilliams, A. Misharin, D. A. Hume, H. Perlman, B. Malissen, E. Zelzer, S. Jung, Fate mapping reveals origins and dynamics of monocytes and tissue macrophages under homeostasis. *Immunity* **38**, 79–91 (2013). doi:10.1016/j.immuni.2012.12.001 Medline

24. S. Safaiyan, N. Kannaiyan, N. Snaidero, S. Brioschi, K. Biber, S. Yona, A. L. Edinger, S. Jung, M. J. Rossner, M. Simons, Age-related myelin degradation burdens the clearance function of microglia during aging. *Nat. Neurosci.* **19**, 995–998 (2016). doi:10.1038/nn.4325 Medline

25. E. O. Samstad, N. Niyonzima, S. Nymo, M. H. Aune, L. Ryan, S. S. Bakke, K. T. Lappegård, O.-L. Brekke, J. D. Lambris, J. K. Damås, E. Latz, T. E. Mollnes, T. Espevik, Cholesterol crystals induce complement-dependent inflammasome activation and cytokine release. *J. Immunol.* **192**, 2837–2845 (2014). doi:10.4049/jimmunol.1302484 Medline

26. C. Oberle, J. Huai, T. Reinheckel, M. Tacke, M. Rassner, P. G. Ekert, J. Buellesbach, C. Borner, Lysosomal membrane permeabilization and cathepsin release is a Bax/Bak-dependent, amplifying event of apoptosis in fibroblasts and monocytes. *Cell Death Differ.* **17**, 1167–1178 (2010). doi:10.1038/cdd.2009.214 Medline

27. N. Snaidero, W. Möbius, T. Czopka, L. H. P. Hekking, C. Mathisen, D. Verkleij, S. Goebbels, J. Edgar, D. Merkler, D. A. Lyons, K.-A. Nave, M. Simons, Myelin membrane wrapping of CNS axons by PI(3,4,5)P3-dependent polarized growth at the inner tongue. *Cell* **156**, 277–290 (2014). doi:10.1016/j.cell.2013.11.044 Medline

28. D. Lütjohann, C. Hahn, W. Prange, T. Sudhop, M. Axelson, T. Sauerbruch, K. von Bergmann, C. Reichel, Influence of rifampin on serum markers of cholesterol and bile acid synthesis in men. *Int. J. Clin. Pharmacol. Ther.* **42**, 307–313 (2004). doi:10.5414/CPP42307 Medline

29. K. M. Thelen, K. M. Rentsch, U. Gutteck, M. Heverin, M. Olin, U. Andersson, A. von Eckardstein, I. Björkhem, D. Lütjohann, Brain cholesterol synthesis in mice is affected by high dose of simvastatin but not of pravastatin. *J. Pharmacol. Exp. Ther.* **316**, 1146–1152 (2006). doi:10.1124/jpet.105.094136 Medline